Special issue review article

NMR IN BIOMEDICINE

Received: 06 October 2014, Revised: 26 December 2014, Accepted: 13 January 2015, Published online in Wiley Online Library: 23 February 2015

(wileyonlinelibrary.com) DOI: 10.1002/nbm.3268

W(h)ither human cardiac and body magnetic resonance at ultrahigh fields? technical advances, practical considerations, applications, and clinical opportunities

Thoralf Niendorf[a,b]*, Katharina Paul[a], Celal Oezerdem[a], Andreas Graessl[a], Sabrina Klix[a], Till Huelnhagen[a], Fabian Hezel[a], Jan Rieger[c], Helmar Waiczies[c], Jens Frahm[d,e], Armin M. Nagel[f], Eva Oberacker[a] and Lukas Winter[a]

The objective of this study was to document and review advances and groundbreaking progress in cardiac and body MR at ultrahigh fields (UHF, $B_0 \geq 7.0$ T) with the goal to attract talent, clinical adopters, collaborations and resources to the biomedical and diagnostic imaging communities.

This review surveys traits, advantages and challenges of cardiac and body MR at 7.0 T. The considerations run the gamut from technical advances to clinical opportunities. Key concepts, emerging technologies, practical considerations, frontier applications and future directions of UHF body and cardiac MR are provided. Examples of UHF cardiac and body imaging strategies are demonstrated. Their added value over the kindred counterparts at lower fields is explored along with an outline of research promises.

The achievements of cardiac and body UHF-MR are powerful motivators and enablers, since extra speed, signal and imaging capabilities may be invested to overcome the fundamental constraints that continue to hamper traditional cardiac and body MR applications.

If practical obstacles, concomitant physics effects and technical impediments can be overcome in equal measure, sophisticated cardiac and body UHF-MR will help to open the door to new MRI and MRS approaches for basic research and clinical science, with the lessons learned at 7.0 T being transferred into broad clinical use including diagnostics and therapy guiding at lower fields.

Keywords: magnetic resonance; MRI; ultrahigh field; cardiovascular imaging; body imaging; heteronuclear MR; MR technology; RF coils

* *Correspondence to: T. Niendorf, Berlin Ultrahigh Field Facility (BUFF), Max-Delbrueck Center for Molecular Medicine, Berlin, Germany.*
E-mail: thoralf.niendorf@mdc-berlin.de

a *T. Niendorf, K. Paul, C. Oezerdem, A. Graessl, S. Klix, T. Huelnhagen, F. Hezel, E. Oberacker*
Berlin Ultrahigh Field Facility (BUFF), Max-Delbrueck Center for Molecular Medicine, Berlin, Germany

b *T. Niendorf*
DZHK (German Centre for Cardiovascular Research), Partner Site, Berlin, Germany

c *J. Rieger, H. Waiczies*
MRI.TOOLS GmbH, Berlin, Germany

d *J. Frahm*
Biomedizinische NMR Forschungs GmbH, am Max-Planck-Institut für biophysikalische Chemie, Göttingen, Germany

e *J. Frahm*
DZHK (German Centre for Cardiovascular Research), Partner Site, Göttingen, Germany

f *A. M. Nagel*
Medical Physics in Radiology, German Cancer Research Center (DKFZ), Heidelberg, Germany

Abbreviations used: *λ, wavelength; ε, permittivity; σ, electrical conductivity; ^{1}H, hydrogen protons; ^{23}Na MRI, sodium MRI; ^{31}P MR, phosphorus magnetic resonance; ATP, adenosine triphosphate; B_0, main magnetic field strengths; B_1^+, electromagnetic transmission field; $BaSrTiO_3$, barium strontium titanate; BMI, body mass index; BMR, body magnetic resonance; CAI, coronary artery imaging; CMR, cardiac magnetic resonance; CP-like, circularly polarized-like; D_2O, deuterium oxide; DREAM, dual refocusing echo acquisition mode; DWI, diffusion weighted imaging; ECG, electrocardiography; EMF, electromagnetic field; f, frequency; FLASH, fast low angle shot; FOV, field of view; FSE, fast spin-echo; GRAPPA, generalized autocalibrating partially parallel acquisitions; HS8, hyperbolic secant RF pulse with (n=8); IEC, International Electrotechnical Commission; MRA, magnetic resonance angiography; MRC, magnetic resonance cholangiography; NA, number of averages; Na^+, sodium; NaCl, sodium chloride; PCr, phosphocreatine; PINS, power independent number of slices; R_1, longitudinal relaxivity; R_2, transversal relaxivity; RFPA, RF power amplifier; RX, RF reception; SAR, specific absorption rate; SNR, signal-to-noise ratio; T_E, echo time; TE_{01} mode, transverse electric mode 01; TIAMO, time-interleaved acquisition of modes; T_R, repetition time; TX, RF transmission; UHF-MR, ultrahigh field magnetic resonance; UISNR, ultimate intrinsic signal-to-ratio; VIBE, volume Interpolated Breath-hold Examination; VOPs, virtual observation points.*

INTRODUCTION

The growing number of reports referring to technology transfer and explorations into body and cardiovascular applications is an inherent testament to the advancements of MR at ultrahigh magnetic field strengths ($B_0 \geq 7.0$ T, $f \geq 298$ MHz). Pioneering explorations into ultrahigh field (UHF) body MR (BMR) document the progress in liver, renal, abdominal, pelvic and prostate imaging and spectroscopy (1–24). Early applications of UHF cardiac MR (CMR) manifest the advances for imaging and spectroscopy of the heart and the large vessels (25–59). These technical and pilot studies respond to unsolved problems and unmet needs of today's clinical BMR/CMR. These developments are fueled by the signal-to-noise ratio (SNR) advantage inherent to higher magnetic field strengths and are driven by explorations into novel MR technology.

The progress is heartening and creates the legitimate temptation to sing the praise of UHF-BMR/CMR. Transferring UHF-BMR and UHF-CMR into the clinic remains a major challenge though (32), since the advantages are sometimes hampered by a number of concomitant physics related phenomena and by practical impediments. It is no secret that these obstacles bear the potential to spoil the benefits of UHF-CMR/BMR. Although reports from clinical early adopters of 7.0 T BMR/CMR remain largely anecdotal at this point, momentum is gathering for broader application oriented feasibility studies and for clinical studies, which will be enabled by increasingly robust and streamlined hardware and software platforms.

Recognizing the technical advances and clinical opportunities of UHF-BMR/CMR together with the need for broader clinical studies, this review is an attempt to make the (bio)medical and diagnostic imaging communities aware of this productive ferment, so as to engage the interest of potential clinical adopters, to inspire collaborations across disciplinary boundaries and to attract basic scientists, engineers, hardware professionals, translational researchers, applied scientists and new entrants into the field; with the goal to advance the capabilities of UHF-BMR/CMR by fostering explorations into the many remaining unresolved problems and technical obstacles. In the sections that follow, examples of enabling UHF-BMR/CMR technology and their applications are provided. Encouraging developments into multiple channel RF concepts are reviewed. Advances in imaging methodology and progress in RF pulse design are discussed. Early and frontier applications of BMR/CMR at 7.0 T are surveyed together with the clinical opportunities for high spatial resolution MR, parametric mapping, MR angiography (MRA) and real time imaging, all being facilitated by the properties of ultrahigh field magnetic resonance (UHF-MR). Liver, renal and prostate UHF-BMR applications are presented. Heteronuclear UHF-BMR/CMR applications are explored, including sodium MR and phosphorus MR. Practical considerations of UHF-BMR/CMR are outlined. The subjective acceptance during UHF-BMR/CMR examinations is discussed. Insights into RF heating induced by conductive stents and implants along with RF power deposition considerations are provided. Current trends in UHF-BMR/CMR are considered together with their clinical implications. A concluding section ventures a glance beyond the horizon and explores future directions. Of course, ultrahigh field BMR/CMR is an area of vigorous ongoing research, and many potentially valuable developments will receive only brief mention here.

TECHNICAL SOLUTIONS FOR ULTRAHIGH FIELD BODY AND CARDIAC MR

Enabling RF coil technology

At ultrahigh fields the crux of the matter is that the wavelength becomes sufficiently short versus the size of the upper torso, abdomen and pelvis. As deep-lying organs surrounded by the lung, stomach, bowels and other inhomogeneous tissue structures within the comparatively large volume of the thorax, abdomen and pelvis, the anatomy targeted in CMR and BMR is particularly susceptible to non-uniformities in the RF transmission field (B_1^+). These detrimental B_1^+ phenomena can cause shading, massive signal drop-off or even signal void, and hence bear the potential to offset the benefits of UHF-BMR/CMR due to non-diagnostic image quality.

To address this obstruction for broader clinical studies, a plethora of reports eloquently refers to the development of enabling RF technology tailored for BMR and CMR at 7.0 T. In fact, the momentary non-uniformities in the transmission fields in the thorax and abdomen are generally so significant that the use of traditional birdcage body coils at 298 MHz become elusive if not prohibitive. This need has inspired explorations into novel RF technology including cardiac and body optimized multi-channel coil array configurations. Research directions include (i) local transceiver (RF transmission/RF reception, TX/RX) arrays and (ii) multi-channel transmission arrays in conjunction with multi-channel local receive arrays.

Arguably, the wide spectrum of BMR/CMR applications ranges from large volume imaging to localized spectroscopic probing, which renders the design of a single optimal many-element RF coil configuration elusive. Obviously, the selected RF coil design should first of all meet the requirements of patient safety, patient comfort and ease of clinical use to harmonize the technical specifications with the clinical needs. This includes light weight, flexibility, capability to accommodate multiple body habitus and anatomical variants, and a modular and multi-dimensional arrangement of coil elements or building blocks, together with a sensitive region large enough to cover the target anatomy in the upper torso, abdomen and pelvis (32).

Multi-channel RF coil designs tailored for UHF-BMR/CMR involve rigid, flexible and modular configurations. The gestation process revealed a trend towards a larger number of transmit and receive elements (31,35,37–39,53) to improve anatomic coverage and to advance the capabilities for transmission field shaping (60). Pioneering developments made good use of building blocks that include stripline elements (6,25,26,61,62), elecrical dipoles (46,62–65), dielectric resonant antennas (55) and loop elements (31,35,37–39,53), with the number of independent elements ranging from two to 32.

Loop element based CMR/BMR optimized 7.0 T transceiver configurations were reported for a four-channel TX/RX design that is equipped with two anterior and two posterior elements (Fig. 1(a)) (35). An alternative loop array comprises eight TX/RX channels split into five anterior and three posterior elements (Fig. 1(b)) (37). Both configurations make use of a one-dimensional arrangement of the elements. This setup constrains the degree of freedom for transmission field optimization and for parallel imaging. A two-dimensional arrangement of loop elements uses 16 TX/RX channels with the elements being distributed to eight anterior and eight posterior elements, both arranged in a 2×4 array (Fig. 1(c)) (39). This approach was extended to a more sophisticated modular 32-channel TX/RX array, shown in Fig. 1(d) (53). This configuration comprises four planar (posterior section) and four modestly shaped (anterior section)

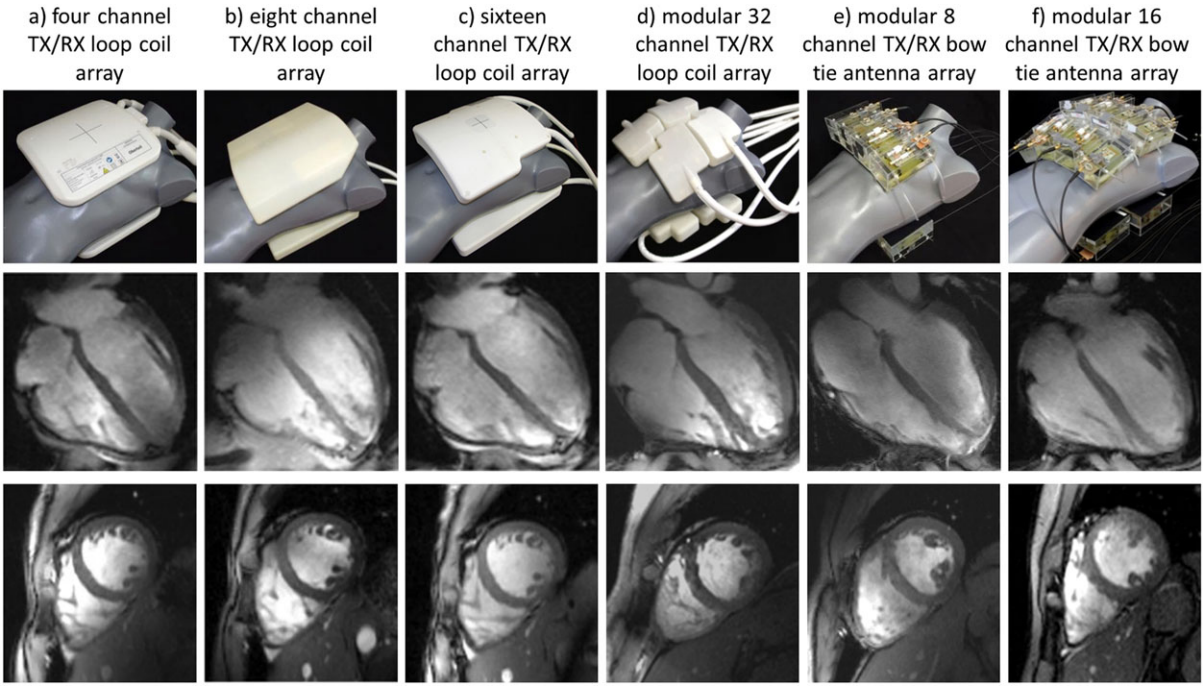

Figure 1. Examples of multi-channel transceiver arrays tailored for CMR at 7.0 T. Top: photographs of cardiac optimized 7.0 T transceiver coil arrays including (left to right) a four-channel, an eight-channel, a 16-channel and a 32-channel loop array configuration together with an eight-channel and a 16-channel bow tie antenna array. For all configurations the elements are used for transmission and reception. Middle, bottom: four-chamber (middle) and short axis (bottom) views of the heart derived from 2D CINE FLASH acquisitions using the RF coil arrays shown at the top and a spatial resolution of (1.4 × 1.4. × 4.0) mm^3.

modules (53), each module being fitted with four independent transceiver loop elements (2 × 2 array).

Various stripline element based 7.0 T transceiver configurations were proposed for cardiac and body UHF-MR. In a pioneering eight-element transverse electromagnetic field (TEM) transceiver array design, each element was independently connected to a dedicated RF power amplifier (RFPA) (25). Other stripline array configurations run flexible designs consisting of a pair of four (Fig. 2(a)) or eight stripline elements, one placed anterior and the other posterior to the torso (26,61). Another practical solution comprising an eight-channel stripline transceive array (Fig. 2(b)) that uses sophisticated automated tuning with piezoelectric actuators was accomplished (54).

Electric dipoles have been shown to be suitable for CMR and BMR at 7.0 T, including deep seated targets such as the prostate and the pelvis (46,63). Electric dipoles show the trait of a linearly polarized current pattern, where RF energy is directed perpendicular to the dipole along the Poynting vector to the subject, resulting in a symmetrical, fairly uniform excitation field with increased depth penetration (63). Early implementations include straight dipole elements (63). To enable efficient power transmission from dipole antennae, the length of the antenna needs to be adjusted to the transmission frequency, so the antenna size can be as long as 35–50 cm for a straight, self-resonant half wavelength dipole antenna at 297 MHz. This geometry is suitable for large volume body MRI at 7.0 T but imposes a constraint (i) for the design of many-element, two-dimensional transceiver arrays confined to cardiac fields of view and (ii) for parallel imaging along all standard and multi-oblique cardiac views. The need for densely packed multichannel transceiver coil arrays tailored for UHF-BMR/CMR inspired explorations into electric dipole configurations that comprise eight or 16 bow tie antenna building blocks as shown in Fig. 1(e), (f). Each of the building blocks contains a bow tie shaped $\lambda/2$-dipole antenna immersed in D_2O (46), which is an MR inactive molecule with a permittivity of $\varepsilon \approx 81$ at 298 MHz. This approach helps to shorten the effective antenna length. To establish a CMR/BMR array of 16 independent TX/RX channels, eight bow tie antenna building blocks were combined to form an anterior and a posterior coil section, each in a 4 × 2 array (Fig. 1(f)).

Improvements in the compactness of dipole antenna arrays were also accomplished by incorporating lumped element inductors, by using fractionated dipoles (Fig. 2(c)) or by employing meander structures (66–68). The requirements of UHF-BMR/CMR along with ultimate intrinsic SNR and current pattern considerations inspired alternative dipole antenna designs. One important development is bent electric dipoles (69). Other configurations include circular dipoles, which consist of a circular conductor with a feed point on one side and a gap on the other (70). Recently proposed dipole antenna variants include folded dipoles (71).

Another conceptually very appealing building block design is the dielectric resonant antenna fabricated with high permittivity, low loss ceramics (55). These building blocks are designed to operate in the TE_{01} mode at 298 MHz (55). This resonance mode dictates the disc geometry, which for example resulted in a diameter of 86 mm and a height of 39 mm for $BaSrTiO_3$ resonators with a relative permittivity of 165 (55). Inductive coupling using a small non-resonant coupling loop for each resonator was applied for impedance matching and for coupling energy into the ceramic resonator. To form an eight-element transceiver array, four building blocks were placed on top of the anterior chest while four building blocks were positioned posterior to the upper torso (Fig. 2(d)).

To summarize, stripline elements, dielectric resonant antennae, loop elements and electric dipoles are valuable building blocks for local transceiver coil configurations customized for BMR and CMR

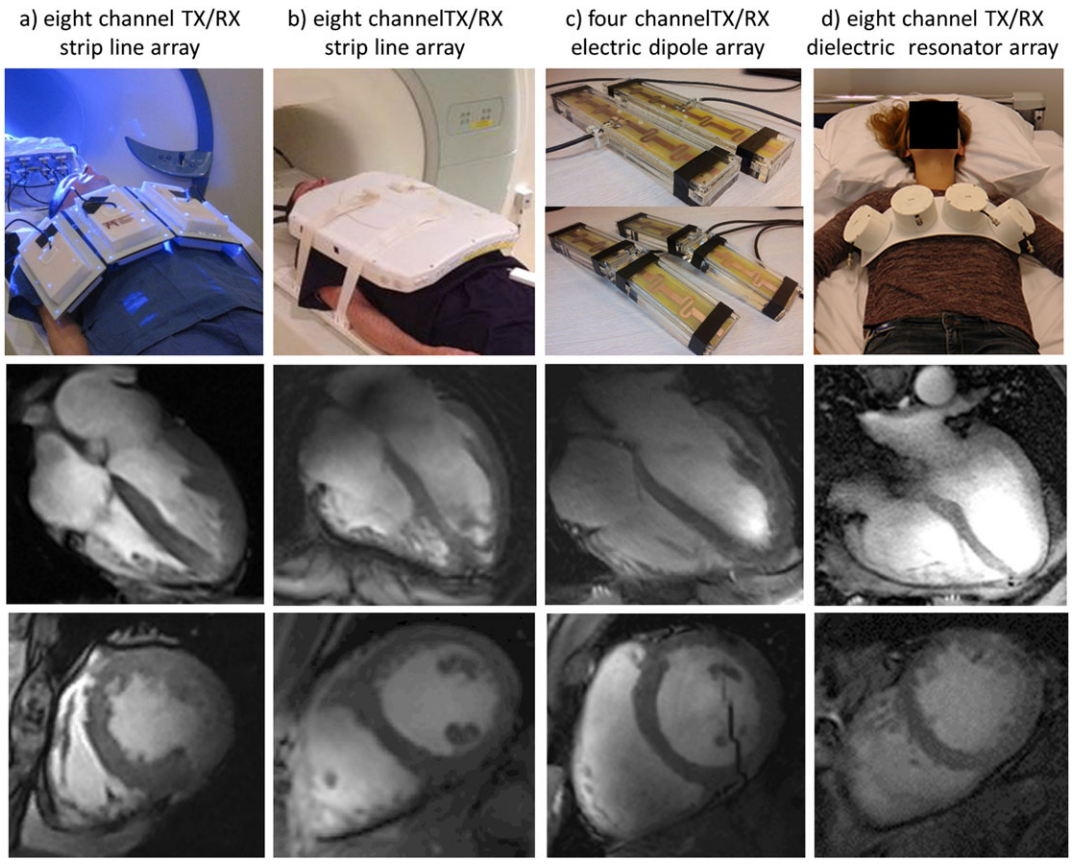

Figure 2. Examples of multi-channel transceiver arrays tailored for CMR at 7.0 T. Top: photographs of (a) an eight-channel stripline array (61), (b) an eight-channel stripline array that uses automated tuning with piezoelectric actuators (54), (c) a four-channel electric dipole antenna array using fractionated dipoles along with meander structures (66–68) and (d) an eight-channel dielectric resonant antenna array fabricated with high permittivity, low loss ceramics (55). Middle, bottom: four-chamber (middle) and short axis (bottom) views of the heart derived from 2D CINE FLASH acquisitions using the RF coil arrays shown at the top. Images courtesy of (a) Mark E. Ladd, Stefan Maderwald and Oliver Kraff, Erwin L. Hahn Institute, University Duisburg-Essen, Essen, Germany, (b) Matthew D. Robson, Radcliffe Department of Medicine, University of Oxford, Oxford, UK, (c) Alexander Raaijmakers, Department of Radiotherapy, University Medical Centre Utrecht, Utrecht, The Netherlands, and (d) Sebastian Aussenhofer, C. J. Gorter Center for High Field Magnetic Resonance, Leiden University Medical Center, Leiden, The Netherlands.

at 7.0 T. To this end ultimate intrinsic signal-to-noise ratio (UISNR) considerations outlined that loop and dipole current patterns contribute equally to UISNR at 7.0 T (72,73). For field strengths of $B_0 \geq 9.4$ T current patterns are dominated by linear (dipole type) current patterns (72,73), which provides motivation for shifting the weight to dipoles versus loop and stripline elements.

Multi-channel RF chain

To translate the capabilities of multi-channel RF coil configurations into practical value advances in MR systems hardware abounded. Contemporary UHF-MR system architecture supports multi-channel transmit arrays to be driven in two modes, using (i) an array of independent feeding RFPAs with exquisite control of phase, amplitude or even complete RF waveforms for all individual channels or (ii) a single-feeding RFPA. For the single-feeding RFPA regime the amplifier output is commonly split into fixed-intensity signals using RF power splitters. Phase adjustments for individual coil elements or groups of coil elements are accomplished with phase shifting networks or coaxial cables. This setup provides a practical solution, which can be made readily available for a large number of MR sites. In today's research implementations RFPAs with up to 16 kW peak power are used for the single-feeding RFPA mode. State of the art multi-feeding RFPA implementations support up to 16 RF amplifiers, each providing up to 2 kW adjustable RF output power. This setup provides software driven control over phase and amplitude by modulating the applied input signal. Moreover, it enables sophisticated parallel transmission of independent RF waveforms to every channel. On the journey to a broader range of UHF-BMR/CMR applications, it is beneficial if RF coil configurations provide flexibility that supports single-feeding as well as multiple-feeding RFPA regimes without major changes in cabling and other components (53).

Advances in imaging methodology

Advances in imaging methodology comprise two main categories for UHF-BMR/CMR: (i) novel approaches for transmission field mapping and (ii) new technologies for transmission field shaping.

The knowledge of the spatial B_1^+ distribution generated by coil arrays is pivotal for UHF-BMR/CMR to manage transmission fields across the target region, including signal excitation, signal refocusing and magnetization preparation. B_1^+ mapping approaches commonly used are mainly magnitude based and are generally confined to the ratios or the fit of signal intensity images (74–81). For this purpose, sets of images are acquired using

either two flip angles (75–77), identical flip angles but different repetition times (T_R) (79), variable flip angles (78,80) or signals from spin echoes and stimulated echoes (74), as well as signals from gradient echoes and stimulated echoes (82). It should be noted that B_1^+ mapping is not a need limited to transceiver arrays tailored for ^{1}H UHF-MR. For instance B_1^+ mapping has been applied to ^{23}Na MRI to support quantification of sodium tissue content (83).

Many of the B_1^+ mapping techniques rely on the knowledge of the steady state magnetization B_1^+ (75). This makes large volume coverage flip angle mapping time consuming, due to the speed constraints dictated by the need for rather long repetition times ($T_R > 5\ T_1$) to avoid T_1 saturation effects. Also, the competing constraints of cardiac and respiratory motion limit the viable window of data acquisition, so B_1^+ mapping of the heart and body is commonly limited to single-slice breath held acquisitions. To address the anatomic coverage and speed constraints, a B_1^+ mapping approach was proposed that is based on a magnetization prepared transient gradient-echo sequence and that facilitates sub-second acquisitions (82). The speed gain renders the dual refocusing echo acquisition mode (DREAM) suitable for large volume coverage multi-slice acquisitions within clinically acceptable breath-hold durations. B_1^+ mapping with DREAM was shown to be adjuvant for liver imaging, which benefits from the improvements in flip angle accuracy and transmission field uniformity over the target volume (84). The sensitivity of DREAM to blood flow is a remaining concern for cardiovascular and body B_1^+ mapping. To offset this sensitivity, a motion sensitized driven-equilibrium magnetization preparation was used, which showed ample suppression of blood signal in the cardiac chambers and in large vessels (85).

Phase based techniques present an alternative for B_1^+ mapping, and were reported to be more accurate versus magnitude based methods for the low flip angle regime (86). These methods commonly make use of a composite or off-resonance RF pulse to encode the spatial B_1^+ information into the phase of the magnetization vector. Most phase based methods, however, make use of non-selective pulses for volume excitation in conjunction with 3D imaging schemes (87–89). This approach results in relatively long acquisition times, which often exceed clinically acceptable breath-hold periods, along with a pronounced susceptibility to respiratory motion artifacts. Realizing these limitations, the feasibility of cardiac gated, single-breath-hold B_1^+ mapping has been demonstrated (90) using a 2D phase based Bloch–Siegert approach (91). The reduction of the duration of the Fermi pulse allowed for short T_R, which enabled scan times accommodated by a single breath-hold. It is a remaining issue that phase based B_1^+ mapping might not be exclusively governed by the phase accrual induced by the composite RF pulse but might also reflect phase contributions due to blood flow and cardiac motion. Preliminary results did not show major changes in the calculated flip angle at the blood–myocardium interface, and hence indicate that blood flow related phase contributions might be minor (90).

Notwithstanding the advances in B_1^+ mapping methodology, transmission field mapping of individual coil elements at 7.0 T has been primarily established for head imaging (92–94), but remains a challenge for UHF-BMR/CMR due to depth penetration constraints and susceptibility artifacts. To cope with this challenge, B_1^+ profiles are often derived from numerical electromagnetic field (EMF) simulations (39,53,95). For this purpose the transmit phases for each coil element are adjusted using iterative algorithms to improve transmission field homogeneity in a region of interest encompassing the heart or the abdomen using a human voxel model (96). To ensure that the relative B_1^+ distributions of the individual coil elements derived from the EMF simulations accord with reality, it is essential that EMF simulations are validated against MR measurements using phantoms filled with a dielectric liquid with dielectric properties that resemble those of the target organ/tissue as outlined in Fig. 3. While the single-feeding RFPA mode provides a practical solution, it comes with the caveat that subject specific B_1^+ shimming is not supported. Hence the applicable range of body geometries and body mass indices (BMIs) is centered around the reference subject or the human voxel model used for B_1^+ optimization. Notwithstanding this drawback, clinically acceptable image quality can be obtained for UHF-CMR for a common range of BMIs without the need for patient-specific adjustments (38,39,53), bringing this technology closer to product development and broader clinical use.

Based upon *a priori* acquired B_1^+ maps derived for all individual transmit channels of a coil array, B_1^+ shimming can be used

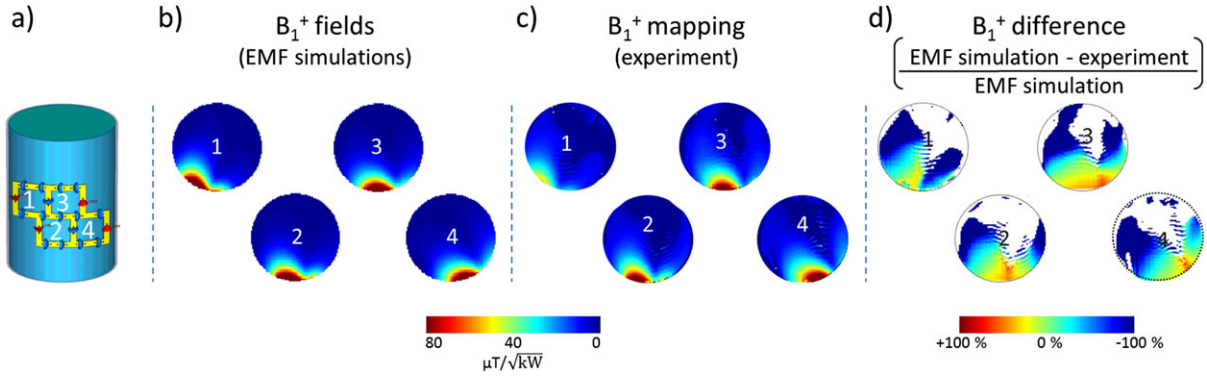

Figure 3. Example of transmission field assessment with EMF simulations and experimental B_1^+ mapping using a building block equipped with four loop RF elements. For this purpose a cylindrical phantom setup was used in the simulations and in the experiments. (a) Virtual model of the setup used for validation (the RF shield and casing are not shown but included in the simulations). The experimental setup was arranged analogously to the virtual setup. (b) Simulated B_1^+ distribution (absolute values) of four channels, which form one curved building block. For B_1^+ evaluation, transversal slices through the cylindrical phantom were positioned in alignment with the center of the loop elements. (c) Absolute transmission fields derived from B_1^+ mapping of the experimental setup. (d) Difference maps as percentages of the simulated results. The results demonstrate the qualitative and quantitative agreement between the numerical simulations and the measurements.

to reduce RF non-uniformities across the torso using the degrees of freedom of multi-channel transmission to shape the transmission field for UHF-CMR/BMR. Figure 4 shows an example for B_1^+ uniformity improvements across a four-chamber view of the heart using a 32-channel TX/RX coil in conjunction with B_1^+ shimming that makes use of (i) a B_1^+ optimized phase setting using 32 elements, (ii) a phase setting for each building block, each comprising four elements, and (iii) a circularly polarized-like (CP-like) phase setting for all elements (53).

The acquisition of two or more time-interleaved images recorded with complementary RF excitation modes is an extension of static RF shimming in the single-feeding RFPA regime (97). This methodology helps to mitigate signal voids due to B_1^+ non-uniformities by combining the B_1^+ spatial RF excitation patterns (98). The enhanced B_1^+ uniformity comes with a scan time or SNR drawback. This spatiotemporal resolution penalty can be offset by combined reconstruction of virtual coil elements in conjunction with parallel imaging techniques (97).

Arguably, the single-RFPA B_1^+ shimming regime is static and offers limited capabilities if more sophisticated and dynamic B_1^+ adjustments are needed to support cascades of B_1^+ shimming stages, including slice-by-slice specific B_1^+ shimming, subject specific B_1^+ trimming or magnetization preparation modules driven by B_1^+ efficiency requirements versus imaging modules governed by B_1^+ uniformity needs. Dynamic shimming is the forte of the multi-feeding RFPA's mode in conjunction with sophisticated pulse sequence developments, which support cascades of dynamic B_1^+ shimming stages that balance the needs of preparation modules common in body and cardiac imaging, such as inversion, fat suppression or blood suppression, pencil beam excitation across the diaphragm for navigator gated respiratory motion compensation and rapid imaging modules. Frontier BMR/CMR implementations of dynamic B_1^+ shimming at 7.0 T include 2D CINE imaging (99), coronary MRA (100), renal MRA (12), 4D flow MRA of the entire aorta (101) and arterial spin labeling perfusion imaging of the kidneys (102), which demonstrated improved excitation efficiency, increased SNR of myocardium and blood or enhanced blood–myocardium contrast, or helped to balance the B_1^+ uniformity with B_1^+ efficiency (103).

Progress in RF pulse design

Multi-channel transmission (104–107) using spoke RF pulses presents a major breakthrough for pulse sequence developments tailored for UHF-BMR/CMR (49). A juxtaposition of the two-spoke approach with B_1^+ shimming revealed an enhanced excitation fidelity or a reduced RF pulse energy for the two-spoke technique (49). This benefit holds the promise to be instrumental for a broader range of CMR applications, including uniform excitation for parametric mapping used for tissue characterization. Current pulse designs for two-spoke parallel transmission RF pulses make use of a single set of B_1^+/B_0 maps though. This approach may not be suitable for subsequent scans acquired at another respiratory phase because of organ displacement, which might induce severe excitation profile degradation. To address this issue, a tailored parallel transmission RF pulse design, which is immune to respiration induced B_1^+/B_0 variations, has been recently proposed (58). In analogy to the CMR implementation, the two-spoke approach can be exploited to mitigate B_1^+ inhomogeneity in target regions encompassing the pelvis, the abdomen or the liver (15). Multi-band spoke pulses afford simultaneous multi-slice acquisitions with enhanced flip angle homogeneity but minimal increase in integrated and peak RF power (108).

On the RF pulse design side, adiabatic RF pulses and composite RF pulses offer a practical solution to offset the B_1^+ uniformity constraints. These RF pulses provide nearly constant flip angles over a wide B_1^+ range, with a common lower limit of approximately 60% of the expected B_1^+. This advantage comes at the cost of RF power deposition. This issue is pronounced for fast spin-echo (FSE) based imaging

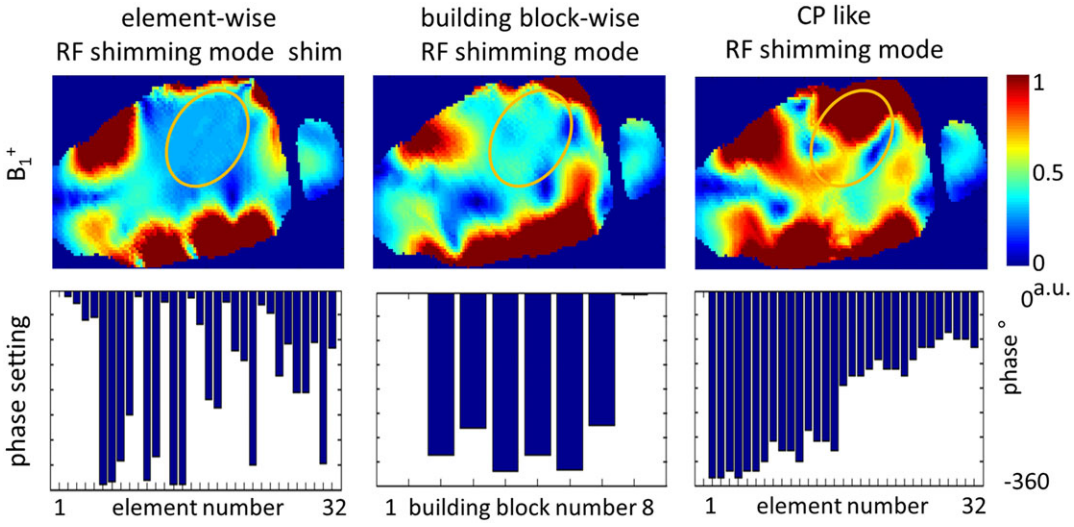

Figure 4. Transmission field shaping using a 32-channel loop element transceiver array (Fig. 1(d)) (53). In this example of static B_1^+ shimming, field shaping is based upon EMF simulations for a multi-oblique plane mimicking a four-chamber view of the heart. Top: B_1^+ field distributions for the three phase setting modes including (left) an element-wise phase setting approach, (center) a block-wise optimized phase setting approach where the phase is set identical for four loop elements forming a four-channel module and (right) a CP-like mode. The element-wise phase setting regime provided the most uniform B_1^+ fields across the heart, which is marked by the orange ellipse. The building-block-wise RF shimming mode provided a more uniform B_1^+ distribution across the four-chamber view of the heart versus the CP-like phase setting regime. Bottom: summary of the phase values used for the three phase setting regimes.

NMR IN BIOMEDICINE

techniques, which exhibit an increased sensitivity to B_1^+ inhomogeneities. The power deposition constraint manifests itself in limited spatial coverage by allowing only a few slices for FSE imaging. To relax this caveat, adiabatic RF pulses are commonly prolonged with pulse durations exceeding 10 ms to reduce peak RF power (17). Obviously, the long inter-echo times put an extra burden onto the point spread function of FSE imaging, which can inadvertently diminish the usefulness of the spatial resolution enhancements of UHF-BMR/CMR. Slice accelerated acquisition schemes using power independent number of slices (PINS) RF pulses that perform spatially periodic excitation and refocusing provide means for relaxing RF power deposition in spin-echo based imaging at 7.0 T (109).

Adiabatic RF pulses were also used in spectrally selective adiabatic RF inversion based fat suppression with the goal to enhance contrast between coronary lumen blood pool and epicardial fat (30). Hyperbolic-secant RF pulses were employed to form a saturation pulse train optimized for first-pass myocardial perfusion MRI at 7.0 T (51).

To deal with respiratory motion in BMR/CMR, prospective navigator gating and tracking using 2D selective pencil beam excitation is another area of activity for RF pulse developments (29). For CMR at 7.0 T, the heart–lung interface rather than the diaphragm is used for navigator localization (29). For this purpose the duration of the 2D selective pencil beam navigator RF pulse was significantly decreased versus protocols established at 3.0 T to master susceptibility artifacts at the heart/lung interface (29).

APPLICATIONS AND CLINICAL OPPORTUNITIES

Cardiac chamber quantification

Early UHF-CMR applications demonstrated the usefulness of 2D CINE spoiled gradient-echo imaging (fast low angle shot, FLASH) for cardiac chamber quantification of the left (28,34,36) and right ventricles (44) at 7.0 T. 2D CINE FLASH provides high quality images with uniform signal intensity distribution and high blood–myocardium contrast over the entire heart, as demonstrated in Fig. 5. Cardiac chamber quantification at 7.0 T agrees closely with left and right ventricle parameters derived at 1.5 T (34).

The baseline SNR gain at 7.0 T can be translated into spatial resolution enhancements versus the counterparts at lower field strengths. Figure 6 surveys four-chamber and short axis views of the heart obtained with a standardized CMR protocol (110,111) and with an enhanced spatial resolution. The latter protocol reduces the voxel size from 19.4 mm^3 to 1.6 mm^3, equivalent to a 12-fold improvement in the spatial resolution versus a standardized clinical CMR protocol. This fidelity approaches an effective anatomical spatial resolution – voxel size per anatomy – that resembles that demonstrated for animal models (112). The overall image quality and improvements in spatial resolution enabled the visualization of fine subtle anatomic structures, including the compact layer of the free right ventricular wall and the remaining trabecular layer. Pericardium, mitral and tricuspid valves and their associated papillary

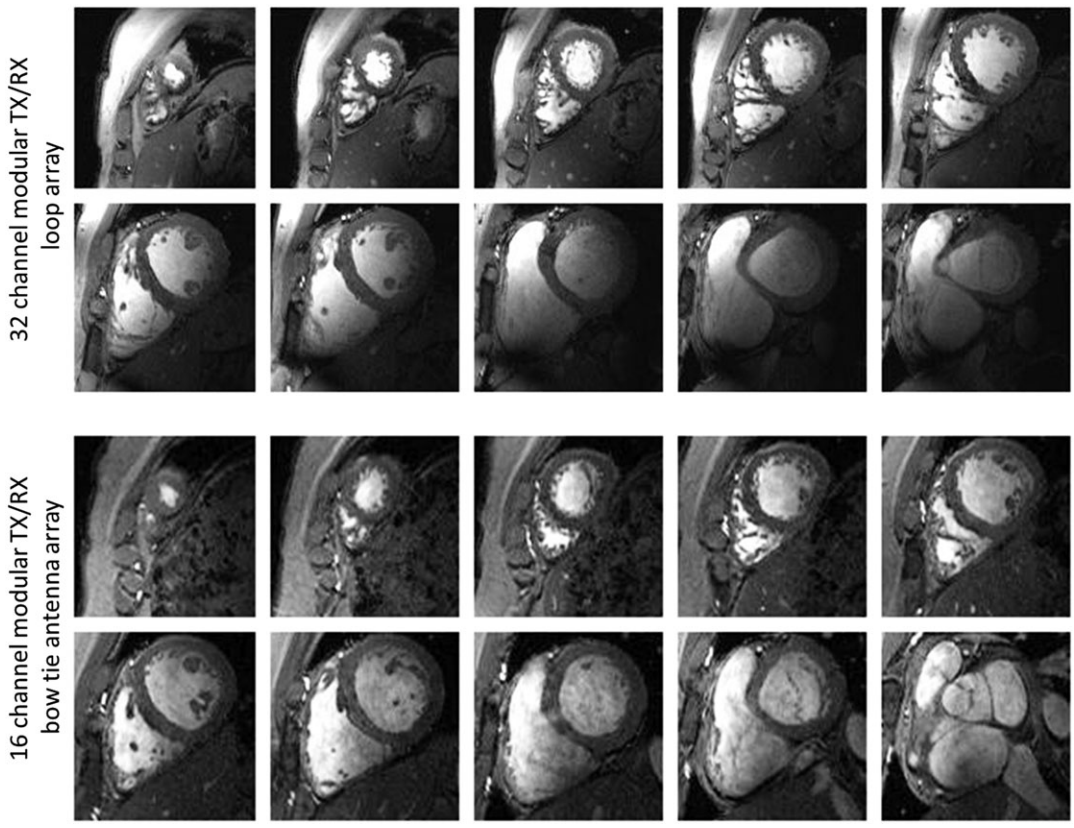

Figure 5. End-diastolic short axis views covering the heart from the apex to the base derived from 2D CINE FLASH imaging (in-plane resolution (1.1 × 1.1) mm^2, slice thickness 2.5 mm, GRAPPA reduction factor 2) using (top) a 32-channel modular TX/RX loop array and (bottom) a 16-channel modular TX/RX bow tie antenna array. Both array configurations provided fairly uniform signal intensity and no major signal voids for slices covering the heart from the apex to the base.

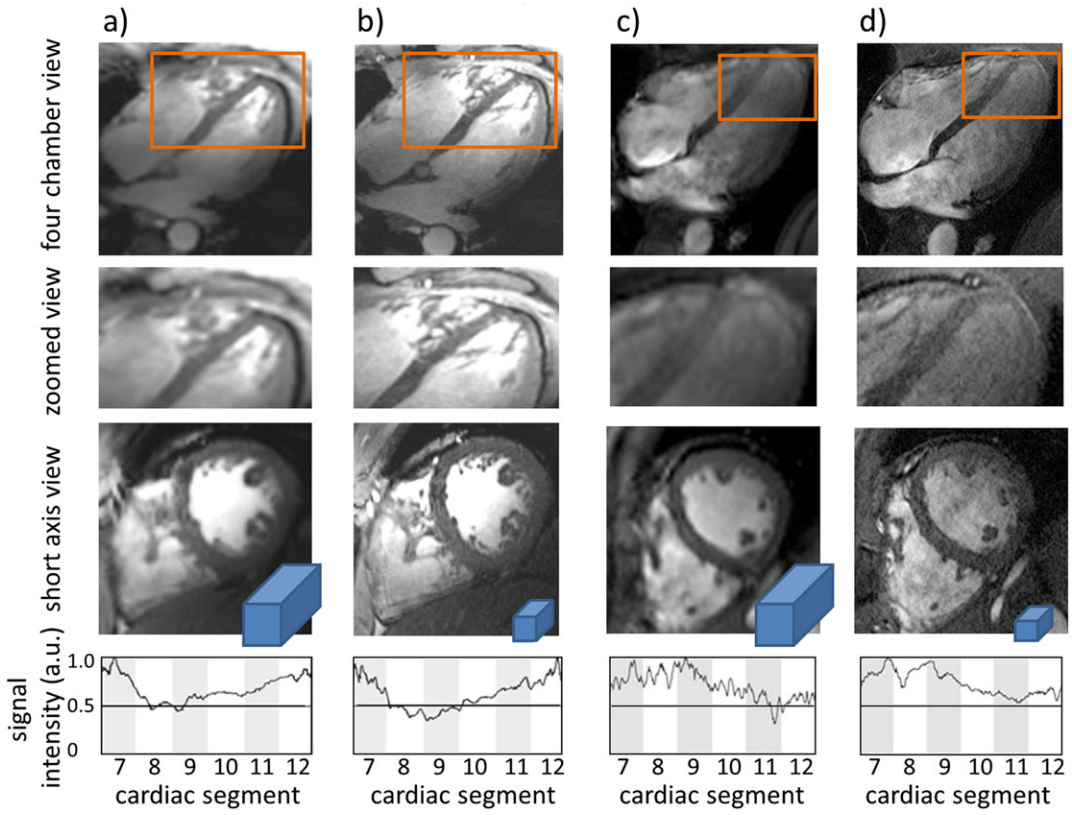

Figure 6. First and third rows: four-chamber views (first row) and short axis views (third row) of the heart derived from 2D CINE FLASH acquisitions (GRAPPA reduction factor 2) using (a), (b) a 32-channel modular TX/RX loop element array (Fig. 1(d)) and (c), (d) a 16-channel modular TX/RX bow tie antenna array (Fig. 1(f)). Different resolutions were employed: (a), (c) standardized clinical protocol – in-plane resolution ($1.8 \times 1.8 \times 6.0$) mm^3, (b) in-plane resolution ($1.1 \times 1.1 \times 2.5$) mm^3 and (d) in-plane resolution ($0.8 \times 0.8 \times 2.5$) mm^3. Second row: magnified views of the ventricular trabeculae, demonstrating that spatial resolution enhancements by a factor of six or even 12 versus standardized protocols used in current clinical practice improve the delineation of subtle anatomical details of the heart. Fourth row: analysis of the signal intensity in the short axis view using a profile along a circular trajectory inside the myocardium.

muscles, and trabeculae are identifiable. For the short axis views a standard deviation of the signal intensity over the myocardium of approximately 20 % was observed.

A recent implementation demonstrated the applicability of slice-selective two-spoke parallel transmit RF pulses in cardiac 2D CINE imaging at 7.0 T (49). For this purpose cardiac gated, breath held B_1^+ multi-channel calibration maps and ΔB_0 maps were acquired to guide the amplitude and phase modulated RF pulse design for each channel. With the two-spoke approach the B_1^+ field was found to be improved significantly for the posterior region of a four-chamber view of the heart including the atria and the large vessels (49). With a two-spoke pulse setting transmitter voltage/RF pulse energy could be increased by 22%/50% to obtain higher blood–myocardium contrast without exceeding the RF power deposition limits (49).

First pass myocardial perfusion imaging

Clinical CMR assessment of ischemic heart disease includes rapid first-pass contrast agent enhanced myocardial perfusion MRI (111). Numerous saturation-recovery based perfusion techniques have been proposed to capture first-pass kinetics with one- or two-heartbeat temporal resolution**.** Saturation methods established at lower fields are suboptimal for myocardial perfusion imaging at 7.0 T (51). To address this issue, a novel saturation pulse train consisting of four hyperbolic-secant (HS8) RF pulses was proposed for effective saturation of myocardium at 7.0 T (51). This approach facilitated an average saturation efficiency of 97.8% in native myocardium and afforded the first series of human first-pass myocardial perfusion images at 7.0 T (51). The ability to produce exquisite in-plane spatial resolution at 7.0 T may offer greater diagnostic value for myocardial perfusion assessment and supports an extension of the perfusion assessment to the right ventricle. With sufficient acceleration and imaging speed, perfusion imaging is on the verge for 3D whole heart coverage acquisitions (113), which might be furthered by the properties of UHF-MR.

Myocardial T_2* mapping

The ability to probe for changes in tissue oxygenation using T_2* sensitized imaging/mapping offers the potential to address some of the spatial and temporal resolution constraints of conventional first-pass perfusion imaging and holds the promise to obviate the need for exogenous contrast agents. For T_2* mapping at 7.0 T a reasonable B_0 uniformity across the heart is key so that susceptibility weighting is not dominated by macroscopic B_0 field inhomogeneities but rather by microscopic B_0 susceptibility gradients (42). A mean peak-to-peak B_0 difference of approximately 65 Hz was found across the left ventricle (42), which compares well with 3.0 T (114) and 1.5 T studies (115). For myocardial anterior, anterolateral and inferoseptal segments,

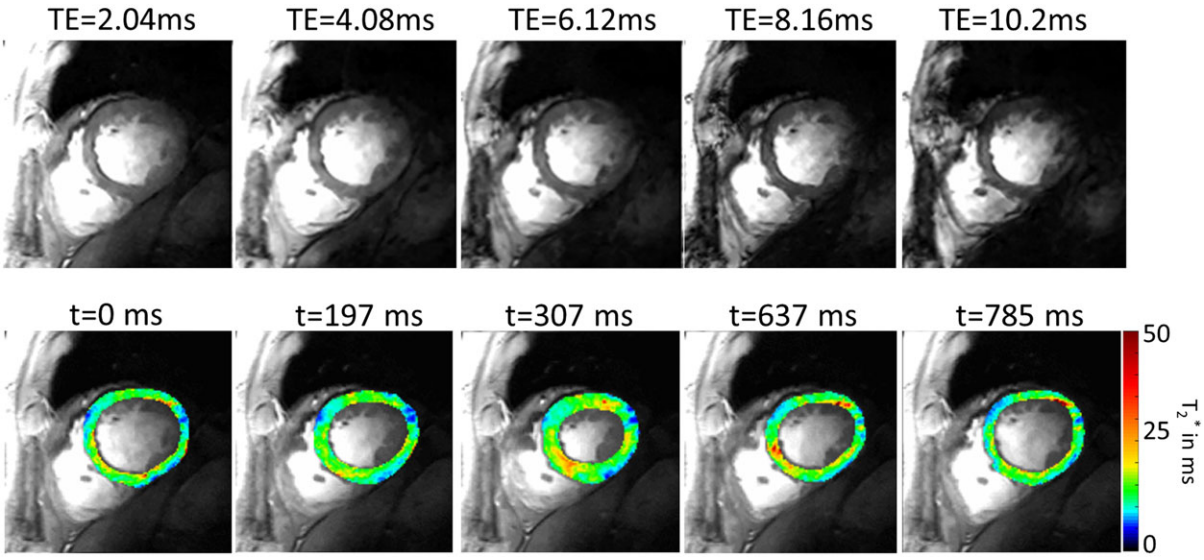

Figure 7. Example of myocardial T_2* mapping at 7.0 T. Top: T_2* weighted short axis views of the heart for a mid-ventricular slice derived from multi-echo gradient-echo imaging at 7.0 T. Images were obtained with the echo times shown. A spatially adaptive non-local means denoising filter was applied (205). Bottom: T_2* color maps of a short axis view of the heart derived from a series of T_2* sensitized 2D CINE acquisitions covering the entire cardiac cycle (five cardiac phases out of a series of 21 cardiac phases are shown) overlaid on conventional 2D CINE FLASH images.

a mean in-plane B_0 gradient of approximately 3 Hz/mm was observed. With this B_0 uniformity high spatial resolution myocardial T_2* mapping at 7.0 T is feasible (42,48), as demonstrated in Fig. 7. The longest mean T_2* values were found for the anterior (T_2* = 17.3 ms), anteroseptal (T_2* = 16.8 ms) and inferoseptal (T_2* = 16.3 ms) segments. Septal segments showed the lowest spatial variation in T_2*, which is similar to that reported for 1.5 T and 3.0 T (48). The inferior (T_2* = 12.0 ms) and inferior lateral (T_2* = 11.4 ms) wall yielded the lowest T_2* values, with the spatial variation being significantly pronounced versus 1.5 T and 3.0 T (48). The 7.0 T setup used facilitated a spatial resolution as good as (1.1 × 1.1 × 2.5) mm^3, which helped to reduce intravoxel dephasing along the slice direction (42).

Detailing magnetic field strength dependence revealed that myocardial T_2* decreases linearly with B_0, with the mean global T_2* of healthy myocardium being approximately 14 ms at 7.0 T versus 27 ms at 3.0 T (116) and approximately 37 ms at 1.5 T (117). This makes the susceptibility effect due to (patho)physiology of interest more pronounced, so T_2* mapping at 7.0 T might be beneficial to address some of the blood oxygenation level dependent (BOLD) contrast imaging sensitivity constraints reported for the assessment of regional myocardial oxygenation changes in the presence of coronary artery stenosis (118). The recent progress in *in vivo* histology and in fiber orientation tracking using T_2* weighted and susceptibility weighted MR (119–121) suggests that the linear relationship between T_2* and B_0 might provide a means to gain a better insight into the myocardial microstructure. Since the susceptibility effects depend on the tilt angle between blood filled capillaries and the external magnetic field strength (115,122–124), T_2* mapping at 7.0 T might contribute to explorations into visualization of myocardial fibers, into the examination of helical angulation of myocardial fibers or into the assessment of fibrotic tissue and other kinds of microstructural tissue change.

To avoid T_2* quantification errors due to signal modulations induced by fat–water phase shift, echo times where fat and water are in phase are commonly used for T_2* mapping (125). This translates into inter-echo times of ΔT_E = 2.2 ms at 3.0 T and ΔT_E = 4.4 ms at 1.5 T. Consequently it is elusive to study temporal changes in T_2* across the cardiac cycle at 1.5 T and 3.0 T due to scan time constraints, which are prohibitive for CINE T_2* mapping covering the cardiac cycle. At 7.0 T ΔT_E governed by the fat–water shift is 1.02ms, which facilitates CINE T_2* mapping customized for T_2* monitoring across the cardiac cycle (Fig. 7) (42). The improved temporal resolution of T_2* mapping at 7.0 T provides a means of monitoring externally controlled variations of blood oxygenation, including short periods of hypoxia and hyperoxia test stimuli (126,127).

Myocardial T_1 mapping

Myocardial tissue characterization using T_1 weighted late gadolinium enhancement imaging is of proven clinical value for the assessment of ischemic heart diseases but also for non-ischemic myocardial diseases (111). T_1 weighted imaging is qualitative and subjective though, which demands advancements towards myocardial T_1 mapping (128–130). At 7.0 T, increased RF transmit power and improved B_0 shimming play complementary roles for myocardial T_1 mapping, which requires careful transmission field shaping and B_0 shimming. This requirement can be managed if quantification of and correction for imperfect inversion is applied (47). For this purpose, an adiabatic inversion pulse tailored for use in the heart in conjunction with a shortened modified look locker inversion variant was employed (47). Subject averaged inversion efficiencies ranging from −0.79 to −0.83 (perfect inversion would provide −1) were accomplished across myocardial segments (47). T_1 of normal myocardium has been reported to be (1925 ± 48) ms at 7.0 T (47) versus (1166 ± 60) ms at 3.0 T (131) and (721 ± 37) ms at 1.5 T (130). The prolonged T_1 relaxation times at 7.0 T provide an enhanced blood–myocardium contrast superior to that at 1.5 T, which afforded a revival of spoiled gradient-echo imaging techniques at 7.0 T. Slice-selective variable flip angle techniques provide an alternative for rapid parametric T_1 mapping (132). This approach obviates the need for

inversion recovery preparation, while being fast enough to meet the speed requirements of CMR.

Fat–water imaging

Fat–water separated cardiac imaging provides a sensitive means of detecting intramyocardial fat, characterizing fibro-fatty infiltration, characterizing fatty tumors and delineating epicardial and/or pericardial fat. Multi-echo Dixon approaches utilizing iterative decomposition have been shown to provide robust fat–water separation even in the presence of large field inhomogeneities (133). Equipped with this technology, fat–water separated imaging at 7.0 T has been demonstrated for cardiac and body applications (134–136).

Coronary artery imaging

CAI remains technically challenging due to small vessel size, vessel tortuosity and physiological motion (137,138). UHF-CAI studies using non-contrast gradient-echo imaging techniques suggested that image quality did already approach that achieved for CAI at 3.0 T (29,30,50). Coronary vessel sharpness at 7.0 T was found to be improved versus 3.0 T (30). The early studies focused primarily on the right coronary. To afford appropriate coverage of all main coronary arteries the capabilities of dynamic B_1^+ shimming were exploited (100). The capabilities of UHF-CAI were furthered by employing high spatial resolution CAI (Fig. 8(a)) (50). For this approach, coronary vessel edge sharpness was found to be superior to the border sharpness accomplished in state-of-the-art CAI at 3.0 T. Visible vessel length and vessel diameter obtained at 7.0 T were competitive with those at 3.0 T (50).

Traditional frequency-selective fat saturation techniques used in CAI might suffer from large static field variations at 7.0 T, which may cause non-uniform and imperfect fat suppression over the target region: an effect that bears the risk of obscuring the delineation of coronary arteries. Here fat–water separated imaging holds the promise to substitute conventional preparatory fat saturation techniques (Fig. 8(b)). This approach also promises to offset some of the RF power deposition constraints that come with conventional saturation recovery based fat saturation, which makes use of large flip angles.

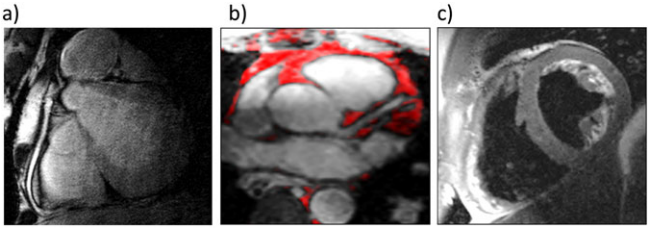

Figure 8. Examples of emerging UHF-CMR applications. (a) High resolution image of the right coronary artery acquired with a spatial resolution of $(0.45 \times 0.45 \times 1.2)$ mm^3, which was facilitated by a navigator gated free breathing 3D gradient-echo acquisition in conjunction with spectrally selective adiabatic inversion recovery at 7.0 T (courtesy of Maurice M. Bizino and Hildo Lamb, Department of Radiology, Leiden University Medical Center, Leiden, The Netherlands). (b) Fat–water separated (gray scale, water image; color scale, fat image) CAI showing the left main coronary artery using the Dixon approach at 7.0 T. (c) Black blood imaging of a short axis view of the heart derived from high spatial resolution ($(0.9 \times 0.9 \times 4.0)$ mm^3) FSE imaging at 7.0 T.

Vascular imaging

MRA of the large vessels is a common cardiovascular MR application. MRA stands to benefit from UHF-MR. The SNR gain can be used to counter the noise amplification caused by acceleration techniques employed to meet the high spatiotemporal resolution requirements of MRA. Potential applications include large volume coverage, time resolved phase velocity MRA (4D flow), which is an emerging technique for studying the flow pattern or wall shear stress in large vessels. The feasibility of aortic 4D flow at 7.0 T was recently demonstrated (56). For this purpose a prospectively gated 4D flow sequence was applied. This approach provided an SNR enhancement of 2.2/3.7 versus 3.0 T/1.5 T for non-contrast-enhanced acquisitions in the descending aorta (56). Another 4D flow MRA implementation at 7.0 T made good use of dynamically applied B_1^+ shimming toggling a setting tailored for the navigator used for respiratory gating and the imaging module (101).

Perhaps UHF-MR forms another important enabling factor to transform the baseline SNR advantage into improved spatiotemporal resolution of contrast enhanced MRA. To this end an SNR gain for contrast enhanced versus non-contrast-enhanced 4D flow MRA was reported to be approximately 1.4 at 7.0 T, which was found to be in accordance to 3.0 T and 1.5 T observations (56). Research continues to examine the impact of prolonged T_1 relaxation times and altered R_1 and R_2 relaxivity of clinically approved gadolinium (III) chelate based contrast media on the blood/background tissue contrast at 7.0 T. These studies include the assessment of contrast agent doses required to accomplish maximal available contrast enhancement (139,140).

Black blood imaging

Transfer of FSE based black blood imaging to 7.0 T is of high relevance for advancing the capabilities of UHF-CMR for explorations into cardiac morphology and myocardial tissue characterization. FSE imaging at 7.0 T presents a special challenge due to the train of high peak RF power refocusing pulses ($\alpha \leq 180°$). Notwithstanding its utility for improving B_1^+ uniformity in UHF-FSE imaging, recent studies on using adiabatic pulses for UHF-FSE reported long inter-echo times of up to 15 ms: an approach that does not meet the CMR requirements.

The feasibility of cardiac FSE imaging at 7.0 T using an eight-channel transceiver array of bow tie antennas (Fig. 1(e)) is demonstrated in Fig. 8(c). For this purpose a spatial resolution of $(0.9 \times 0.9 \times 4.0)$ mm^3 was applied, which represents an order of magnitude improvement versus standardized protocols of today's clinical CMR practice (111). The blood suppression inherent to FSE works well in most regions of the heart. Only slow flowing blood in areas close to the endocardium remains visible. The refinement of black blood preparation modules – including double inversion recovery preparation – tailored for 7.0 T is anticipated to further FSE image quality at 7.0 T. Here a modest diffusion weighting could provide a valuable alternative for spoiling remaining signal induced by slow flowing blood. Figure 8(c) also indicates that the dynamic range of FSE image contrast at 7.0 T is dominated by subcutaneous fat signal despite the applied spectral preparation pulse, which requires further efforts into fat suppression techniques. Alternatively, reduced field of view (FOV) acquisition can be exploited to exclude subcutaneous fat of the chest wall from the FOV. The application of double-echo FSE techniques, which afford a simultaneous combination of

different image contrasts, provides opportunities to advance the capabilities of UHF black blood imaging (141). Generating dual contrast simultaneously within one acquisition offers substantial scan time reduction. This is of benefit in a clinical scenario where multiple parameters/contrasts are assessed. Moreover, simultaneous acquisition of multiple contrasts obviates the need for slice co-registration when combining multiple series of images with anatomical (T_2 or proton density) and functional (diffusion weighted imaging, DWI) contrast, which would be beneficial for CMR dealing with physiological motion. The use of self-calibrated parallel imaging techniques tailored for FSE imaging presents another opportunity to extend the capabilities of black blood imaging at 7.0 T (142). For this purpose the full echo of coherent FSE needs to be decomposed into two parities, which can be independently phase encoded using (i) regular sampling to derive coil sensitivity profiles and (ii) *k*-space undersampling for accelerated FSE acquisitions (142). One practical implication is that the speed gain of self-calibrated FSE would help to reduce examination times, while improving both operator convenience and patient comfort.

Real time imaging

Breath held 2D CINE acquisitions segmented over 10–16 regular heartbeats are the clinical standard for left ventricle structure and function assessment. Yet, the traditional approach is limited by physiological (e.g. cardiac arrhythmias) constraints, which might cause inappropriate diagnostic information. Free breathing real time cardiac MRI achieves diagnostic quality in a single heartbeat (143) and bears the potential to change the landscape of cardiac diagnostics (144–146). These developments will afford an improved clinical accuracy and efficacy of CMR. The accelerated imaging capabilities and the anatomic coverage of multichannel bow tie antenna arrays (Fig. 1(e), (f)) supported free breathing real time imaging of the heart and of the aorta at 7.0 T (Fig. 9). The spatial resolution of (1.2 × 1.2 × 6.0) mm^3 and the frame rate of 30 frames per second fully meet if not exceed the requirements of standardized left ventricular structure and function assessment protocols used in today's CMR practice (111). The real time FLASH images of the aorta demonstrated the extended anatomic coverage of the 16-channel bow tie antenna array along the head–feet direction, including details of the liver and the spine without B_1^+ signal voids (Fig. 9). Real time imaging also provides opportunities for high spatiotemporal resolution UHF-BMR, including tracking abdominal and pelvic movement patterns, and for assessing small bowel disease (147,148).

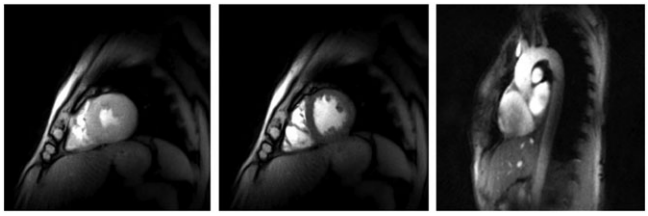

Figure 9. Examples derived from free breathing real time imaging of a mid-ventricular short axis view of the heart (left, systole; center, diastole) using an eight-channel bow tie antenna array (Fig. 1(e)) and of the aorta (right) using an 16-channel bow tie antenna array (Fig. 1(f)). Images were acquired at a rate of 30 frames per second using highly undersampled radial 2D FLASH with nonlinear inverse reconstruction at a spatial resolution of (1.2 × 1.2 × 6.0) mm^3. The real time images of the aorta demonstrate the 35 cm anatomic coverage of the 16-channel bow tie antenna array along the head–feet direction, including details of the liver and the spine without B_1^+ signal voids.

Renal imaging

The potential spatial resolution advantage of UHF-BMR would benefit the evaluation of patients with renal insufficiency, renal tissue hypoperfusion/hypoxia, effects of iodinated x-ray contrast media, or acute kidney injury and its progression to chronic kidney disease, and preoperative evaluation of renal vasculature and anatomy (126,127,149,150). The feasibility of renal MRI at 7.0 T was demonstrated at an early stage of the development process (5). At this stage it was concluded that T_1 weighted gradient-echo MRI provides best image quality and excellent conspicuity of the non-enhanced vasculature, which is beneficial for time of flight MRA (Fig. 10). The feasibility of dynamic contrast enhanced T_1 weighted renal imaging (Fig. 10) was demonstrated (4). Image quality obtained for T_2 weighted FSE imaging was strongly impaired because of signal inhomogeneities.

The evaluation of the potential of high spatial resolution MRA of the renal vasculature using contrast enhanced (4) and non-contrast-enhanced (7) techniques at 7.0 T showed enhanced vessel delineation and vessel conspicuity. First pass perfusion renal MRA revealed an improvement in vessel delineation versus non-contrast acquisitions (11).

In more sophisticated implementations of renal MRA at 7.0 T, dynamically applied B_1^+ shimming solutions were incorporated into a non-contrast-enhanced renal MRA technique that makes use of two B_1^+-shim sets (12): one customized for B_1^+ efficiency maximization to drive contrast preparation and another one tailored for uniform low flip angle imaging (12). This approach supports high resolution imaging of the renal vasculature derived from low flip angle gradient-echo acquisitions.

Numerous (pre)clinical studies have underscored the growing scope of T_2* sensitized renal MRI and its value for the noninvasive assessment of renal oxygenation and perfusion (150). To further the capabilities of renal imaging it is compelling to advance high spatial resolution imaging and T_2* mapping of the kidney at 7.0 T.

Liver imaging

Liver imaging constitutes a growing fraction of clinical MRI, including the assessment of focal liver lesions, diffuse liver disease and liver vessel pathologies. A typical liver examination consists of T_2 weighted imaging with and without fat saturation, and T_1 weighted gradient-echo imaging prior to and following administration of contrast media. Since UHF-BMR is becoming more widespread, its advantages can be potentially exploited to drive the spatial resolution into the sub-millimeter range and to enhance the liver vessel/parenchyma contrast. T_1 weighted imaging of the liver was shown to support whole liver coverage (Fig. 11(a)) and fine details of subtle liver structures without the need for contrast agent application (Fig. 11(b)) (21). Besides the gallbladder and the great vessels, capillaries with diameter of the order of half a millimeter were clearly identifiable due to the superb spatial resolution of (0.3 × 0.3 × 2.5) mm^3 (Fig. 11(c)), which is superior to that commonly achieved in clinical settings at 1.5 T and 3.0 T (135,136). Contrast enhanced T_1 weighted MR cholangiography (MRC) using 3D gradient-echo techniques facilitated a uniform depiction of the intra- and extrahepatic

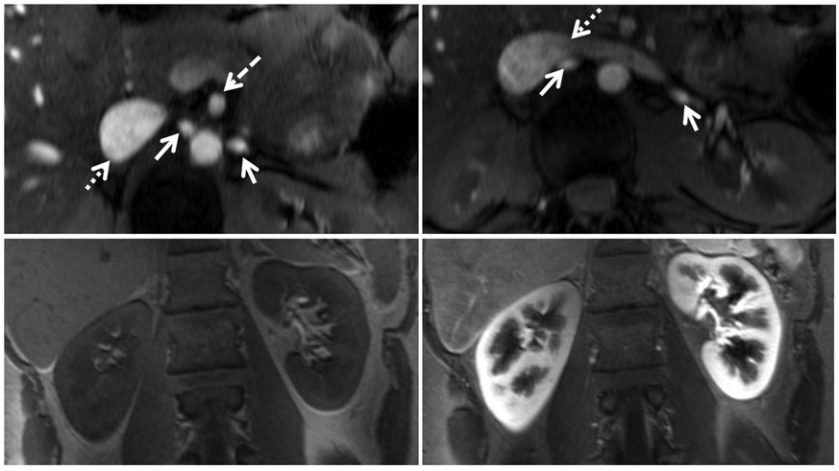

Figure 10. Examples of renal MRI at 7.0 T. Top: TOF-MRA of the renal vasculature. The arrows point to the proximal (left) and peripheral (right) segments of the renal arteries. The dashed arrow points to the superior mesenteric artery. The dotted arrows demonstrate the venous overlay, by means of the inferior vena cava and left renal vein. Bottom: non-enhanced (left) and post-contrast (right, 1 M gadobutrol) T_1 weighted renal VIBE images. (Images courtesy of Lale Umutlu, Erwin L. Hahn Institute for Magnetic Resonance Imaging, University Duisburg-Essen, Essen, Germany.)

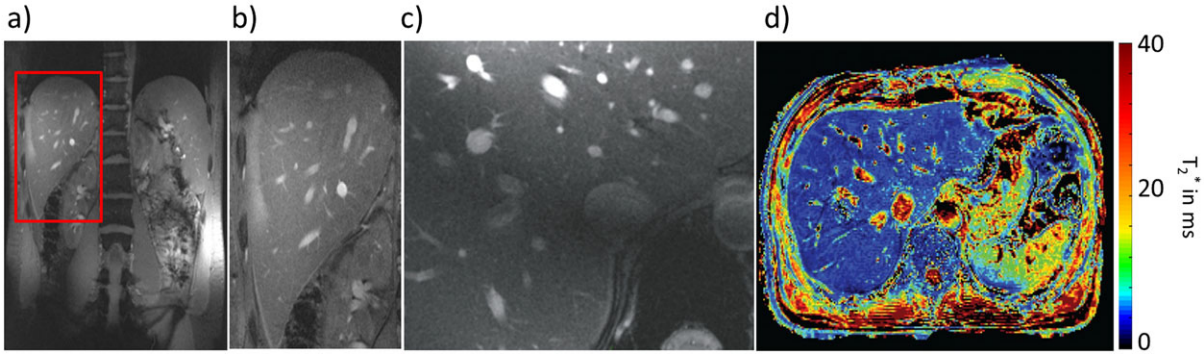

Figure 11. Examples of liver MRI at 7.0 T. (a) T_1 weighted image of a central coronal abdominal slice showing a fairly uniform excitation across the liver. The image was derived from gradient-echo imaging using a 32-channel TX/RX loop array (Fig. 1(d)) and a voxel size of $(0.4 \times 0.4 \times 2.5)$ mm^3. (b) Zoomed view of the area marked in red in (a). (c) Zoomed view of a T_1 weighted axial slice covering the liver, which was derived from gradient-echo imaging using a 16-channel TX/RX loop array (Fig. 1(c)) and a spatial resolution of $(0.3 \times 0.3 \times 2.5)$ mm^3. No contrast agent was applied. Subtle anatomic liver structures are clearly identifiable, including capillaries with a diameter of the order of 0.5 mm. (d) Abdominal T_2* map showing a fairly uniform T_2* distribution across the liver.

biliary tract at 7.0 T, with the depiction of the intrahepatic bile ducts being superior to that of MRC at 3.0 T (19). The use of multi-spoke slice-selective parallel transmit RF pulses would be beneficial for mitigating B_1^+ inhomogeneities observed for liver MRI at 7.0 T (15). Unlike B_1^+ field distribution, B_0 uniformity was found to be acceptable, as indicated by fairly uniform T_2* across the liver (Fig. 11(d)) (135), with T_2* ≈ 10 ms for the parenchyma and T_2* ≈ 10 ms for the large liver vessels.

Liver fat–water imaging was reported to be feasible, with fat and water being correctly classified across the full FOV (135). MR based liver fat and volume could be utilized as endpoints in patients with non-alcoholic fatty liver disease or obesity. It is challenging, though, to incorporate fat–water separation into FSE commonly used for diagnostic T_2 weighted liver and abdominal imaging, which requires uniform fat suppression. To address this issue, a slice-selective gradient reversal technique was applied, which provided uniform fat suppression with moderate tissue signal loss of approximately 20% (18). This approach was combined with the time-interleaved acquisition of modes (TIAMO) technique (97), which facilitated delineation between fat and bright liquids in single-shot FSE (18). The progress in FSE imaging of the liver at 7.0 T opens opportunities for DWI of the liver free of geometric distortion, which is elusive for DWI-EPI (echo planar imaging) because of susceptibility induced distortions. Working in this direction would provide a means for evaluating hepatic fibrosis.

Prostate imaging

Indications for MRI of the prostate include the evaluation of prostate cancer and MRI guided prostate biopsy (151–154). The sensitivity gain at 7.0 T holds the promise to obviate the use of endorectal coils for prostate MRI. Early explorations into prostate MRI at 7.0 T demonstrated high quality images facilitated by transceiver arrays in conjunction with patient specific local B_1^+ shimming (2). With this signal homogeneity and spatial resolution, clear delineation of anatomical features in the prostate and surrounding structures, including the neurovascular bundle, the rectum, the urethra, the transition zone, the peripheral zone and the fibromuscular tissue, was achieved (2). Careful

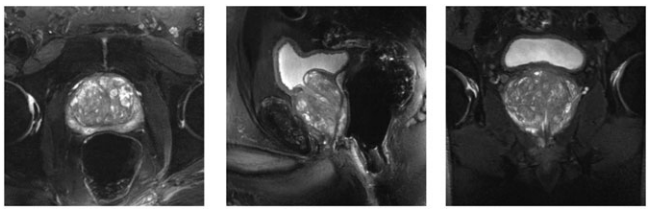

Figure 12. Axial (left), sagittal (center) and coronal (right) T_2 weighted images of the prostate of a patient (weight 98 kg, age 58 years, PSA 6 ng/ml) at 7.0 T (courtesy of Tom W. J. Scheenen, Department of Radiology, Radboud University Medical Centre, Nijmegen, The Netherlands). For data acquisition an FSE imaging technique was used: T_R = 3000 ms, T_E = 71 ms, FOV = (240 × 180) mm^2, matrix 320 × 240, in-plane spatial resolution = (0.75 × 0.75) mm^2, phase encoding direction anterior–posterior, slice thickness = 3 mm, slice gap = 0.6 mm, interleaved slice acquisition, nine echoes, echo spacing 17.8 ms, readout bandwidth 116 Hz/pixel, number of averages (NA) = 1, total acquisition time < 2 min. To reduce RF power deposition, a prolonged 150^0 RF pulse was used for refocusing. An eight-channel external stripline array was used for TX/RX and B_1^+ shimming was applied.

examination of the B_1^+ efficiency and B_1^+ uniformity of an endorectal coil and an eight-element microstrip transceiver array at 7.0 T suggested the use of the microstrip array for T_1 and T_2 weighted prostate imaging, whereas the endorectal coil was considered to be the best choice for spectroscopic studies (6). Further advancements in B_1^+ efficiency and uniformity together with a fourfold reduction in local RF power deposition and a 40% SNR increase in the center of the prostate were accomplished by adding an extra stripline element to the conventional endorectal coil (9). The lessons learned from these developments culminated in high quality T_2 weighted FSE imaging of the human prostate using an external transceive body array coil (17) in healthy subjects and in patients with prostate cancer (Fig. 12) (17). This pioneering study demonstrated that prostate tumors diagnosed or confirmed with MR guided biopsy or prostatectomy were well visualized with 7.0 T MRI (17).

Sodium MRI

Sodium MRI (^{23}Na MRI) is an emerging approach for gaining better insights into cellular metabolism, with a broad spectrum of biomedical imaging research applications (155). Previous studies eloquently reported credible data on ^{23}Na MRI of the heart and demonstrated that ^{23}Na MRI is suitable for the detection and assessment of acute and chronic heart disease (156). The rapidly decaying ^{23}Na signal and the low sensitivity of ^{23}Na MRI versus ^{1}H MR constitute a challenge for clinical ^{23}Na CMR. Once clinically feasible, sodium MRI holds the promise to become a valuable diagnostic tool for classifying viable from non-viable tissue in ischemic infarct patients. Recognizing the sensitivity gain and yet unimpaired transmission field homogeneity (43) due to the comparably low ^{23}Na resonance frequency, which is close to that of ^{1}H MRI at 1.5 T, it is conceptually appealing to pursue cardiac ^{23}Na MRI at 7.0 T at clinically acceptable acquisition times. To approach this goal, a local four-element transceiver RF surface coil customized for cardiac ^{23}Na MR at 7.0 T was employed to derive ^{23}Na images of the heart (Fig. 13) with a resolution of (6 × 6 × 6) mm^3 using a density adapted 3D radial acquisition technique (157). These efforts also demonstrated that the sensitivity gain at 7.0 T enables CINE ^{23}Na imaging of the beating heart using a temporal resolution of 100 ms supported

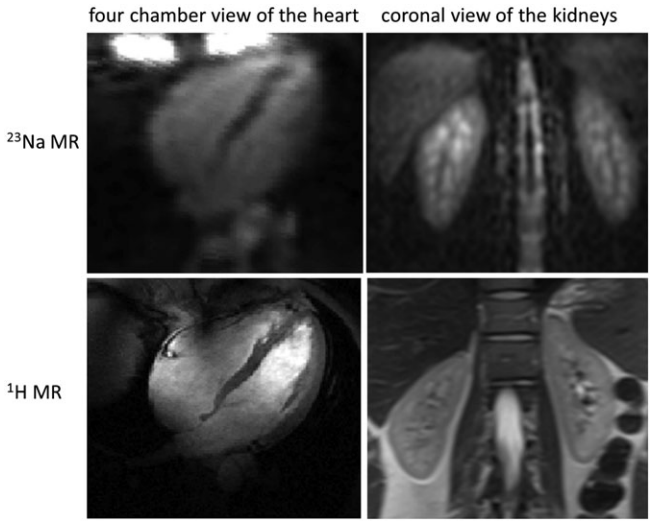

Figure 13. Top: ^{23}Na images of a four-chamber view of the heart (left) and a coronal view of the kidneys (right) acquired at 7.0 T. The ^{23}Na image of the heart was acquired using a density adapted 3D radial technique (157) with T_E = 0.4 ms, T_R = 11 ms, T_{RO} = 7.1 ms, TX amplitude 115 V (~90% SAR), equivalent to a tip angle of 30–40°, number of projections = 50 000, NA = 2 and a voxel size of (6 × 6 × 6) mm^3. The ^{23}Na image of the kidneys (courtesy of Stefan Haneder, Institute of Clinical Radiology and Nuclear Medicine, University Medical Center Mannheim, Heidelberg University, Heidelberg, Germany) was acquired with a spatial resolution of (4 × 4 × 5) mm^3 using a 3D Cartesian spoiled gradient-echo sequence with a variable echo time scheme and a highly asymmetric readout (FOV = (256 × 256) mm^2; matrix size = 64 × 64; number of slices = 24; echo time (T_E) = 4.19 ms; T_R = 49 ms, total scan time = approximately 40 min). Bottom: ^{1}H four-chamber view of the heart (left) derived from 2D CINE gradient-echo imaging at 7.0 T and ^{1}H coronal view of the kidney obtained at 3.0 T (right).

by retrospectively gated, density adapted 3D projection reconstruction (158).

Beyond viability imaging, ^{23}Na MR promises to change the landscape for monitoring Na^+ disposition in the body, which is important in cardiovascular research. A high dietary salt (sodium chloride) intake and the metabolic syndrome are the driving forces for risk factors of the cardiovascular epidemic. Sodium metabolism is closely linked mechanistically to the metabolic syndrome. Na^+ can be bound to proteoglycans that are particularly abundant in the skin. Earlier determinations of skin and muscle Na^+ concentrations in humans were reduced to chemical analysis following excision of material. Such an approach is not clinically acceptable. This state of affairs suggests assessment of sodium content using UHF-MR. The spatial resolution enhancements over 3.0 T setups revealed for the first time the enormous Na^+ content of the human skin, with a millimeter in-plane spatial resolution and less than 11% intra-subject variability (83,159). It stands to reason that the combination of high resolution ^{1}H UHF-MR and sophisticated ^{23}Na MR image reconstruction techniques that include prior knowledge from ^{1}H MRI will enable even higher spatial resolutions for ^{23}Na MR (160).

^{23}Na MRI has been also employed to examine renal sodium content at 7.0 T (Fig. 13). These efforts showed that renal ^{23}Na concentration increases from the cortex in the medullary pyramid direction (20). ^{23}Na T_2* relaxation times were reported to differ between the cortex (17.9 ± 0.8 ms) and medulla (20.6 ± 1.0 ms) (20). This affords the use of clinical imaging protocols built

on gradient-echo techniques, which would be beneficial for translating renal ^{23}Na MRI into broader *in vivo* studies at 7.0 T.

The preliminary results suggest that ^{23}Na MRI at 7.0 T can help to unlock questions regarding Na^+ balance and Na^+ storage functions of kidney, skin and muscle, with the ultimate goal to provide imaging means for diagnostics and for guiding treatment decisions in cardiovascular and metabolic diseases.

Phosphorus MR

Phosphorus MR affords *in vivo* insights into the energy metabolism, and is an ideal candidate to benefit from the sensitivity gain and improved frequency dispersion at higher fields. To demonstrate the sensitivity gain, careful juxtaposition between cardiac ^{31}P MRS at 7.0 T and 3.0 T was conducted (52). These pioneering studies revealed marked superiority of cardiac ^{31}P spectra at 7.0 T relative to 3.0 T (Fig. 14). SNR improvements of 2.8 for phosphocreatine (PCr) (52) together with a reduced standard deviation for the PCr/adenosine triphosphate (ATP) ratio were observed. This gain resulted in an enhanced quantification accuracy at 7.0 T. Myocardial ^{31}P T_1 relaxation times are shorter at 7.0 T versus 3.0 T. These improvements could permit scan time reductions versus 3.0 T and might eventually allow metabolic probing of dynamic processes. For all these reasons it was concluded that 7.0 T will become the field strength of choice for cardiac ^{31}P MRS tailored for probing myocardial energy metabolism (52).

Probing phosphorylated metabolites with ^{31}P MRS can be also used for prostate cancer characterization at 7.0 T (13). ^{31}P spectroscopic imaging using an endorectal coil together with adiabatic excitation enabled the acquisition of phosphorus spectra covering the entire prostate with a spatial resolution of 4 cm^3 in 18 min (10) or of 5.1 cm^3 in approximately 9 min (Fig. 14). This achievement supported the detection of phosphocholine, phosphoethanolamine and inorganic phosphate, which could serve as MR based biomarkers for prostate cancer diagnostics. An exploratory study involving 15 patients with biopsy-confirmed prostate cancer showed distinct features of phospholipid metabolites in the prostate gland and its surrounding structures (22). However, no differences in the phosphorus metabolite ratios were found between prostate cancer and normal-appearing prostate tissue (22). These observations warrant optimization of ^{31}P MRS technology, including RF coil developments, evaluation of T_1 relaxation times and detailing the impact of the nuclear Overhauser effect of phosphorus-containing metabolites at 7.0 T (23).

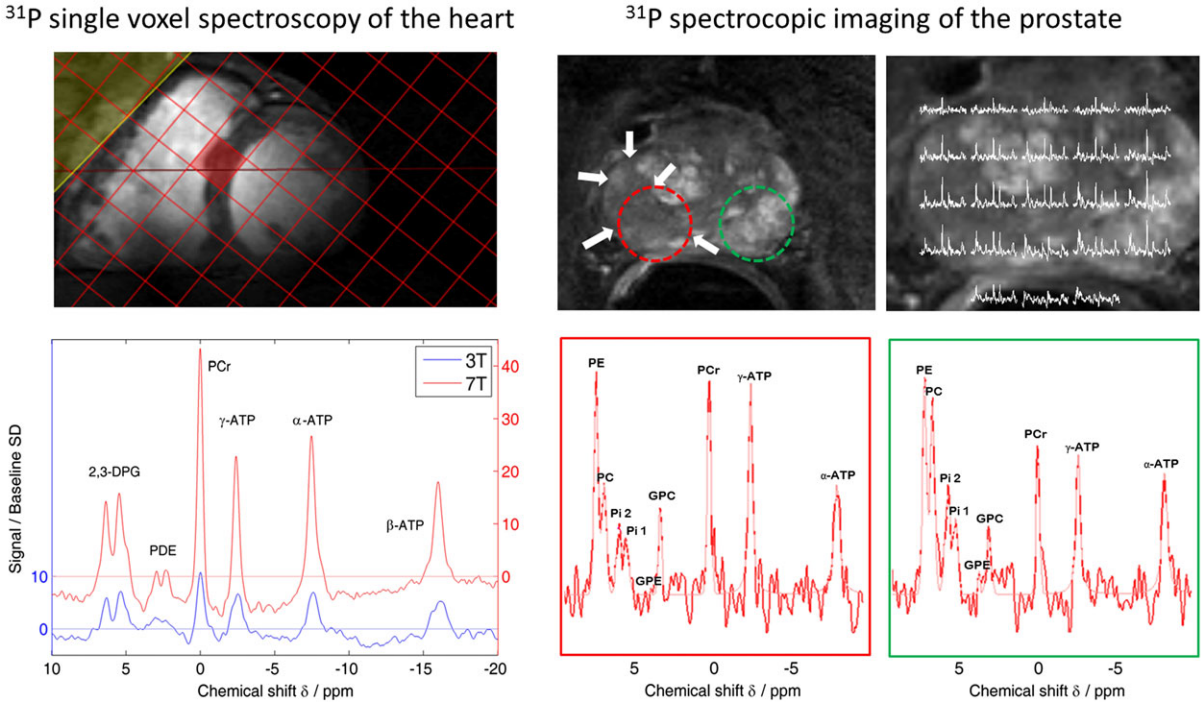

Figure 14. Examples of ^{31}P MRS (left) of the heart (courtesy of Christopher Rodgers, Radcliffe Department of Medicine, University of Oxford, Oxford, UK) and (right) of the prostate (courtesy of Tom W. J. Scheenen, Department of Radiology, Radboud University Medical Centre, Nijmegen, The Netherlands). Left: Comparison of single-voxel ^{31}P spectra of the human heart obtained at 3.0 T and at 7.0 T. The voxel used for ^{31}P MRS was placed in the middle of the interventricular septum, as illustrated in the short axis view of the heart obtained from a 2D CINE FLASH localizer scan at 7.0 T. ^{31}P MRS at 7.0 T provided an SNR advantage over ^{31}P MRS at 3.0 T. Right: ^{31}P spectra of a 72-year-old patient with prostate cancer (Gleason score, 4 + 5; volume, 1.5 cm^3) in the peripheral zone on the right-hand side of the gland. The tumor lesion is indicated by white arrows on the transversal T_2 weighted image. The spectral map shows good quality of ^{31}P spectra across the whole prostate. ^{31}P spectra of the tumor (red circle, red frame) and a healthy region (green circle, green frame) are shown separately with the following resonances: phosphoethanolamine (PE), phosphocholine (PC), two phosphate peaks (Pi1 and Pi2), glycerophosphoethanolamine (GPE), glycerophosphocholine (GPC), phosphocreatine (PCr), gamma-ATP and alpha-ATP. ^{31}P spectra were derived from spectroscopic imaging using a pulse acquire sequence with a 45 degree adiabatic excitation BIR-4 pulse (duration = 8 ms), T_R = 1.5 ms, FOV = (120 × 120 × 120) mm^3; matrix size = 10 × 10 × 10, NA = 12, resulting in voxel volumes of 5.1 cm^3 after apodization with a Hanning filter of the *k*-space weighted sampling. Total acquisition time was 9 min 51 s.

NMR IN BIOMEDICINE

PRACTICAL CONSIDERATIONS

Ancillary devices

Physiological motion and flow constraints dictate the viable window for data acquisition in CMR/BMR. Cardiac motion is commonly dealt with using electrocardiography (ECG) gating techniques. ECG, being an electrical measurement, is corrupted by interference with EMFs and by magneto-hydrodynamic effects (40). As UHF-MR becomes more widespread, the significance of artifact sensitivity of ECG recordings increases, and with it the motivation for a practical hardware solution. To this end an MR stethoscope, which builds on the phonocardiogram and which is immune to interference with EMFs, has been proposed and evaluated for the pursuit of robust and safe cardiac gated/triggered UHF-CMR (27,33,161,162).

BMR and CMR applications involve the injection of contrast media. Contrast agent application is most effective and reproducible using a power injector versus manual injection. While many power injectors customized for MR are approved for use at 1.5 T and 3.0 T, assessment and certification of safety, functionality, flow rate, volume and timing fidelity remains an open task at 7.0 T. The electro-mechanical injector components positioned in the 7.0 T environment are of particular safety concern, since the fringe field is stronger and larger versus a clinical 1.5 T or 3.0 T system. Hence it is prudent to mount the powerhead on the wall inside of the scanner room. This approach might come at the cost of an increased length of the supply lines over a 1.5 T and 3.0 T setup. This issue can be fixed through recalibration of the power injector.

Subjective acceptance of UHF-BMR/CMR examinations

On the journey to broader clinical UHF-BMR/CMR applications, it is of relevance to scrutinize how UHF-CMR examinations are tolerated by subjects. Practical concerns evoked by the physical size and mere length of today's 7.0 T MR scanner and the paucity of data about ergonomic constraints, (dis)comfort and sensory side effects are driving the notion that UHF-BMR/CMR constitutes a challenge for subject tolerance of 7.0 T examinations *per se*. Realizing the lack of data, a recent study examined the subjective acceptance during UHF-CMR in a cohort of 165 healthy subjects (59). A questionnaire was used to examine the participant's experience prior to, during and after the UHF-CMR examination. Transient muscular contraction was documented in 12.7% of the questionnaires (59). Muscular contraction was reported to occur only during periods of scanning with the magnetic field gradients being rapidly switched. Dizziness during the study was reported by 12.7% of the subjects (59). Taste of metal was documented by 10.1% of the study population. Light flashes were outlined by 3.6% of the entire cohort. 13% of the subjects reported side effects/observations that were not explicitly listed in the questionnaire but covered by the question about other side effects and observations (59). No severe side effects such as vomiting or syncope after scanning occurred. No increase in heart rate was observed during the UHF-CMR exam versus the baseline clinical examination. To summarize, UHF-CMR examinations are well tolerated by healthy subjects. Broader observational and multicenter studies including patient cohorts with cardiac diseases are required to gain further insights into the subjective acceptance of UHF-CMR examinations.

RF power deposition considerations

RF pulses used in MR applications at low and high magnetic fields deposit RF power in tissue, which can be described by the specific absorption rate (SAR):

$$\mathrm{SAR} = \frac{\sigma \left| \vec{E} \right|^2}{\rho} \qquad [1]$$

with the tissue conductivity σ, the root mean square of the electric field $\vec{E}$ and the tissue density ρ. Excessive SAR levels might lead to elevated temperature levels, making a careful SAR evaluation mandatory to confirm compliance with the RF power deposition limits given by the International Electrotechnical Commission (IEC) standard 60601-2-33:2010 Ed.3 (163) for safe operation of transmit RF coils tailored for UHF-CMR/BMR (163). For this purpose it is circumspect that the safety assessment, the implemented safety measures, the technical documentation and the risk management file for the RF coil are evaluated and made available for implementation in clinical studies following a review and conformity declaration – confirming compliance with the relevant sections of IEC 60601-2-33:2010 Ed.3 and IEC 60601–1:2005 Ed.3. – issued by an independent notified body rather than solely conducting an in-house assessment. In-house procedures make it challenging to comply with a standard since they may vary among institutions, depend on the different level of local expertise, might be compromised by the use of not clearly defined reference values and arbitrary tolerances for key parameters governing RF safety and last but not least are not independent. A notified body is an accredited test laboratory that is independent from manufacturer or distributor and that has been approved by an independent third party to perform tests within a defined test scope for medical devices, and hence is entitled to examine whether a product or procedure complies with the requirements of a certain standard or an equivalent standard document.

The IEC 60601-2-33:2010 Ed.3 technical standard defines limits for whole body average SAR (normal mode, 2.0 W/kg; first level controlled mode, 4.0 W/kg), which is used for large volume body RF coils commonly used for transmission at 1.5 T and 3.0 T. RF power deposition of local transceiver RF coil arrays used for UHF-BMR/CMR is limited by a more restrictive local SAR of 20W/kg for the trunk in first level controlled mode. This restriction implies (i) that the applicable RF power based on local SAR limits is lower than that based on whole body or partial body SAR (164,165) and (ii) that more power has to be applied in order to reach the same flip angle. In addition, electrical conductivity is frequency dependent and increases for UHF-MR. This leads to a direct SAR increase as seen from Equation [1], and an indirect SAR increase due to lower absolute B_1^+ per input power resulting from higher transmission losses in tissue.

At UHF-MR the wavelength becomes sufficiently short versus the upper torso/abdomen/pelvis, which affects the *E*-field distribution inside the body and offsets some of the SAR predictions governed by (166)

$$\mathrm{SAR} \propto \frac{B_1^2 B_0^2 \tau_{\mathrm{RF}}}{m_i T_{\mathrm{R}}} \qquad [2]$$

RF power deposition is substantially affected by the geometry of the upper torso, by positioning of the RF coil with respect to the torso and the heart, by the RF coil design and by

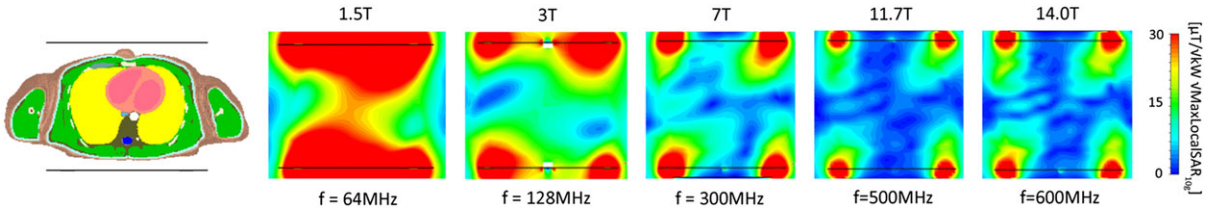

Figure 15. B_1^+ distribution and RF power deposition derived from EMF simulations at 1.5 T, 3.0 T, 7.0 T, 11.7.0 T and 14.0 T using a four-channel TX/RX loop array and the torso of the human voxel model "Duke". For each field strength B_1^+ efficiency distribution is scaled to the maximum local SAR. For each configuration identical phase settings are used for B_1^+ and local SAR (10 g average, 1 W input power) calculations. The $B_1^+/\sqrt{\text{kW}}/\sqrt{\text{max local SAR}_{10g}}$ distribution is shown for 64 MHz, 128 MHz, 300 MHz, 500 MHz and 600 MHz and normalized to an efficiency of 30 $\mu\text{T}/\sqrt{\text{kW}}\sqrt{\text{W/kg}}$. B_1^+ uniformity is substantially reduced for the short wavelength regime for $B_0 \geq 7.0$ T. For the maximum input power of the coils, which is dictated by MR safety regulations that forbid overriding of maximum local SAR, a lower B_1^+ field is generated while moving from 1.5 T to 14.0 T. This demonstrates that a higher average power is required for the excitation pulse to reach the same flip angle at higher MR frequencies. Given a higher average power and assuming that T_R is not prolonged, RF power deposition is shown to be significantly enhanced at UHF-MR frequencies ranging between 300 MHz (7.0 T) and 600 MHz (14.0 T).

the number of TX channels as well as by the RF driving conditions. Here EMF simulations are essential to provide an insight into the local SAR distribution. Figure 15 illustrates the $B_1^+/\sqrt{\text{kW}}/\sqrt{\text{max local SAR}_{10g}}$ distribution for a cardiac optimized four-channel TX/RX array for field strengths ranging from 1.5 T to 14 T. For this purpose the TX/RX array was placed onto the anterior and posterior upper torso of the human voxel model "Duke" (96). For this configuration a lower B_1^+ is achieved for the given local SAR values when moving to higher frequencies. Consequently, a higher RF power deposition is needed to achieve the same flip angle at higher fields. For the setup simulated, a SAR increase by a factor of 13.7 was observed for the mid-ventricular septum when moving from 1.5 T to 7.0 T. In comparison, the same myocardial region showed a factor of 3.5 SAR increase when moving from 7.0 T to 14.0 T. For an apical region a SAR increase of factor 8.1 was derived when moving from 1.5 T to 7.0 T and factor of approximately 2.2 was deduced for a B_0 increase from 7.0 T to 14.0 T. The increase in local SAR to achieve the same flip angle is not as pronounced as reported for a single loop cardiac coil (167). This underlines that local SAR depends on the geometry of the torso/abdomen/pelvis, on the position of the coil with respect to target anatomy, on the RF coil design and on the number of TX channels as well as on the RF driving conditions.

A change in amplitude and phase of each individual transmit channel – commonly used for B_1^+ shimming (1) or parallel transmission (104–107) – may induce significant alterations in local SAR. This behavior generates a need for explorations into concepts for SAR characterization of multi-channel transmission, which is relatively new territory. While commercial configurations of multi-channel transmission at 3.0 T are already CE marked and FDA cleared, multi-channel transmission configurations at 7.0 T are still investigational devices. This constitutes a major road blocker *en route* to a broader range of UHF-BMR/CMR parallel transmission applications, since the primary responsibility for safe use is shifted by the MR manufacturers to the end-users, which creates an asymmetry since it constitutes a subtly but importantly different situation than for "cleared" devices, where this primary responsibility falls to the manufacturers. This asymmetry provides stimulation to the imaging community to throw further intellectual weight behind the solution of the remaining issues. To achieve this goal, strategic research driven by joint efforts of thought leaders from industry, scientists and clinicians should be devoted to the development of enhanced practical solutions for SAR assessment of multi-transmit configurations. In this light patient safety concepts and algorithms were recently proposed for SAR characterization of multi-channel transmission, including EMF simulations using human anatomical models to pre-calculate the electric field distributions of each individual channel (168–170). While being a valuable approach its main limitations are twofold: (i) SAR assessment is based exclusively on human voxel model simulations, which may or may not reflect the specific situation of the given subject, and (ii) the concept does not contain any provisions for RF waveforms deviating from those included in the calculations due to hardware infidelities or hardware malfunction. In this context a novel, comprehensive RF safety strategy for parallel transmission MR was recently put forward (171). The proposed approach allows (i) SAR prediction prior to the scan and (ii) SAR supervision during the scan, and hence provides means for offsetting SAR overestimation while still meeting the requirements of RF safety (171). For this purpose the comprehensive strategy comprises three stages: (i) SAR prediction using preprocessed numerical simulation data obtained for human body models derived from fat–water separated MRI of heathy volunteers positioned in supine position with the arms parallel to the torso; (ii) a preparation phase, where active decoupling and load compensation are used to ensure the predicted SAR matches the actual SAR applied to the subject; (iii) supervision during the scan (171). The latter ensures that global and local SAR limits are not exceeded and that the RF waveforms applied are correct as predicted (171).

On-the-fly SAR calculations including determination of momentary RF amplitudes and phases during the scan, real-time calculation of local SAR maxima and interruption of TX if SAR limits are exceeded constitutes a challenge. To address this issue, several methods that significantly reduce the complexity without restriction to particular RF excitations were proposed (172–176). In a particular implementation it was demonstrated that by compressing complete body models into limited sets of matrices it is sufficient to consider only so-called virtual observation points (VOPs) and still obtain an adequate, conservative estimation of the maximum local SAR (173). The VOPs approach affords substantial processing time savings for maximum local SAR evaluation, and hence holds the promise to support online SAR assessment using pre-calculated electric fields of any arbitrary TX array configuration tailored for UHF-BMR/CMR. Ideally, the models used for simulations of electric fields to be delivered to the VOPs interface should involve subject specific geometry and tissue composition (177), resulting in individualized body SAR models that include conductive implants and devices.

Although SAR is key for RF safety evaluations, temperature distribution – which is the cause of tissue damage based on RF heating – does not follow SAR in a straightforward manner (164). Thermoregulation and heat transfer inside the body (i.e. blood vessels) need to be considered while moving towards a more realistic scenario. Ongoing research focuses already on temperature modeling instead of SAR models, suggesting a thermal tissue damage threshold CEM43 (cumulative equivalent minutes at 43 °C) known from thermal therapies (178,179). Here realistic thermal modelling based on EMF simulations and MR thermometry is essential to assess thermal distributions *in vivo* (180,181). These explorations will help to advance towards enhanced MR safety assessment for UHF-BMR/CMR. This development is expected to include a drive towards controlled E-field steering and targeted SAR reduction technologies in electrically conductive implants, catheters and guide wires using parallel transmission to create excitations that induce minimal RF current in elongated conductors (182,183). An open minded look reveals that UHF-CMR parallel transmission technology perhaps forms an enabling platform to advance interventional CMR applications at 7.0 T by using an MR antenna array to deliberately focus RF power in a controlled way (46). In this context potential applications could include (i) targeted RF guided drug release and image guided monitoring (184), (ii) localized contrast agent release and tracking or (iii) stem cell delivery to the myocardium afforded by local RF heating. One could even conduct a gedankenexperiment where targeted RF heating driven by multi-transmit UHF-MR technology is utilized in thermal therapies or even used for RF ablation versus today's invasive intracardiac catheter ablation.

RF heating of conductive devices

En route to broader clinical UHF-BMR/CMR studies, it is essential to gain a better insight into the interaction of passive conducting implants with RF fields. Considering an ever increasing population of patients with a history of stent implantation, detailing the interaction of stents with RF fields is of profound relevance for the advancement of UHF-BMR/CMR. This is not an easy task because of the many RF coil and stent configurations available, yet becomes even more relevant when moving to many-element transceiver arrays or even to large volume coils covering major sections of the body.

In UHF-MR, the RF wavelength (λ) in myocardial tissue and blood is sufficiently short ($\lambda \sim 12$cm) to induce resonance effects at $\lambda/4$–$\lambda/2$ (185) in coronary stents with a length of up to ~4 cm, a dimension common in clinical practice (186). EMF simulations and RF heating experiments showed that temperature increase due to coronary stents does not exceed baseline RF heating if IEC standards for local and global SAR limits are strictly obeyed (41). While being very important, these early studies did not employ a setup which resembles a clinical scenario (41). The need for RF heating assessment at $B_0 \geq 7.0$ T also prompted valuable research into RF induced heating of metallic arterial stents (187). The conclusions drawn are valuable but constrained to the very specific experimental setup used.

Recognizing the opportunities for broader clinical UHF-MR studies, RF induced heating of coronary stents was examined at 7.0 T (57,188). For this purpose, EMF simulations were performed for a broad range of coronary stent configurations to detail electric fields and local SAR as a function of stent diameter, stent length, stent position with respect to the TX source and stent orientation versus the *E* field (57,188). To translate these results to arbitrary coronary stent geometries, arbitrary stent positions and arbitrary RF coil configurations, an analytical approach for the assessment of EM fields induced in coronary stents was proposed. $SAR_{1\ g}$ induced by a stent ($SAR_{1\ g\ stent}$) can be described by

$$\max\left(SAR_{1g_{stent}}\right) = f(\text{diameter}, \text{length}, \text{orientation})SAR_{1g_{baseline}} \quad [3]$$

with $SAR_{1\ g\ baseline}$ being the local $SAR_{1\ g}$ at the assumed stent position without the presence of a stent (57). Figure 16(b) shows an example of the dependence of induced stent $SAR_{1\ g}$ on stent length and stent orientation versus the *E*-field vector.

The analytical approach provides a fast way to estimate induced stent SAR levels. EMF simulations performed with a stent integrated in a human voxel model prove to be very time consuming. This is a particular practical obstacle if many-element RF TX/RX arrays and a set of phase settings mimicking B_1^+ shimming or other parallel transmit applications are included. Benchmarking the analytical approach versus EMF simulations showed a good conservative estimation of induced $SAR_{1\ g}$ peak levels. A practical example is shown in Fig. 16 using an eight-channel bow tie antenna RF coil array optimized for CMR at 7.0 T (Fig. 1(e)). EMF simulations including the stent consumed more than 2 h CPU (central processing unit) and GPU (graphics processing unit) time per phase setting (not including RF shim field combination and SAR calculations), while the analytical approach can be calculated in real time. This example underscores the value of the proposed analytical approach for obeying regulatory RF power limits (163). The analytical approach is conceptually translatable to other implant configurations and can be conveniently incorporated into state-of-the art SAR prediction concepts (174,189) to provide SAR estimations induced by coronary stents and other conductive implants for arbitrary RF pulses used for transmission field shimming (2,49) or parallel transmission (105,106). To generalize, this approach provides a novel metric or design criteria for RF coils, e.g. to design RF coils (i) with low SAR levels in the vicinity of the stent or (ii) with SAR levels during the presence of the stent which do not exceed SAR levels without the presence of the stent (57).

LOOKING BEYOND THE HORIZON

While today's lion's share of UHF-MR examinations covers brain and neuroscience applications, CMR and BMR are other fields that can benefit from UHF-MR. The eye-opening quality of recent anatomical and functional images has created excitement in the (bio)medical and diagnostic imaging communities and has served as a driving force for application developments, which have culminated in the breadth and detail outlined in this review. This progress is no great surprise, but a number of challenges remain. These unsolved problems should not be hidden under the carpet, but rather act as a surface marker thanks to contributions made by the many forward-thinking researchers, clinician scientists and clinicians. This faith attracts resources, fosters collaborations across the banks of what sometimes appears like a wide river and invites talent, all putting further weight behind solving the conundrum governed by the physics and engineering, with the ultimate goal to harmonize development of novel imaging technology tailored for BMR/CMR with added clinical value, simplicity and ease of use. Meanwhile, the pace

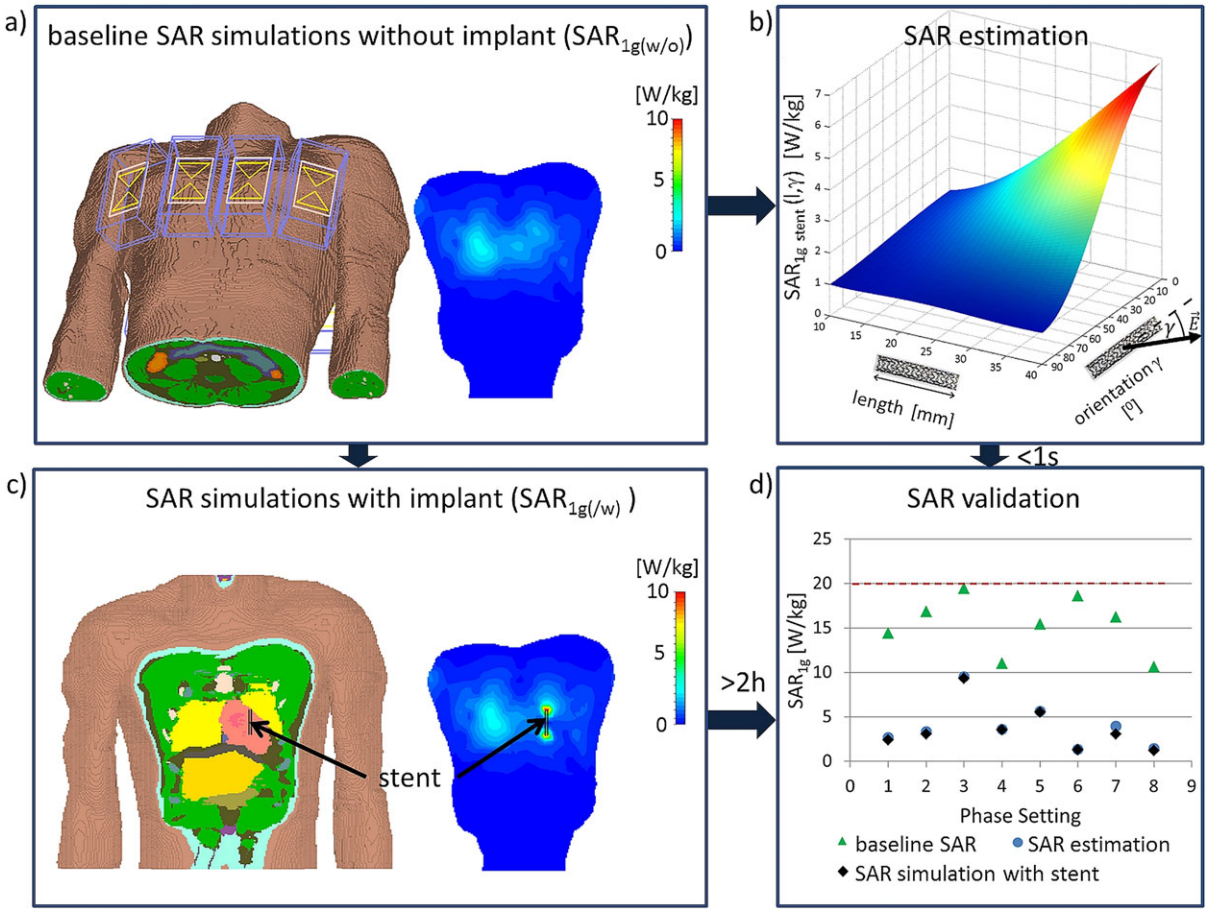

Figure 16. EMF simulations using the human voxel model "Duke" from the virtual family and an eight-channel transmit/receive bow tie electric dipole array. (a) Schematic views of the positioning of the anterior bow tie RF antennas on the anterior chest of the human voxel model and coronal view of $SAR_{1\ g\ baseline}$ distribution for a plane through the target position without the stent equivalent being present. (b) Surface plot of $SAR_{1\ g\ stent}$ derived from Equation [3] for baseline $SAR_{1\ g\ baseline}$ for an input power of 1 W/kg. A stent length ranging from 10 to 40 mm and a stent rotation versus the main *E*-field vector ranging from 0 to 90° was applied. (c) Coronal view of $SAR_{1\ g\ stent}$ distribution for a plane through the target position with the stent equivalent being present. (d) Simulated maximum baseline $SAR_{1\ g\ baseline}$ and $SAR_{1\ g\ stent}$ for the stent equivalent using eight randomly generated phase settings compared with the SAR estimation deduced from the analytical approach (Equation [3]). While conservatively overestimating SAR, SAR estimation using Equation [3] was able to predict the induced $SAR_{1\ g}$ levels without the need to perform extra time consuming EMF simulations with a stent being present in the simulation model.

of discovery is heartening and a powerful motivator to transfer the lessons learned from UHF-BMR/CMR research into the clinical scenario. These efforts are fueled by the quest for advancing the capabilities of diagnostic MRI today: a story worth following, since the implications feed into a broad spectrum of MR physics, biomedical engineering, radiology, cardiology, internal medicine, oncology, nephrology and other related fields of basic research and clinical science (190–193). Moreover, the benefits of 7.0 T BMR/CMR innovations will be more frequently seen at 3.0 T, where the suboptimal copy and paste approach to protocol migration from 1.5 T is being supplanted by the sort of application-targeted redesign that is essential for UHF-CMR/BMR.

An open minded look reveals that the field of UHF-BMR/CMR is in a creative state of flux. It is too early in the exploration stage to make ultimate statements though. Technological advances spurred by the low wavelength regime have already earned UHF-BMR/CMR the label of being a steam engine for innovation along with the recognition of being advanced UHF-MR applications. The requirements of UHF-BMR/CMR are likely to pave the way for further advances in MR technology and MR systems design. With appropriate multi-transmit systems that offer more than 16 TX channels each providing at least 4 kW peak power, an optimistically inclined scientist might envisage the implementation of high density transceiver arrays with 64 and more elements with the ultimate goal to break ground for a many-element upper torso or even a body coil array. This vision continues to motivate new research on integrated multi-channel transmission systems (194) and on RF coil design together with explorations into ideal current patterns yielding optimal signal-to-noise-ratio for UHF-BMR/CMR (72). It is also compelling to embark into the development of high density, multiple-channel on-coil transmit arrays, which would help to reduce the losses in the RF chain (195). The enlarged spectral resolution along with the sensitivity gain stands to boost 7.0 T MR of a broad spectrum of metabolically relevant nuclei including ^{19}F, ^{13}C, ^{17}O, ^{31}P, ^{23}Na, ^{39}K and ^{35}Cl (196–200). This research will drive explorations into metabolic MR and nanomolecular MR probing for which RF coil innovations are to be expected. Perhaps another development is the move toward CMR/BMR using reduced FOVs zoomed into the target anatomy enabled by spatially selective excitation techniques that put the capabilities of parallel transmission technology to good use. Elimination of the information redundancy

intrinsic to today's BMR/CMR applications would change the imaging landscape and would help to offset the complexity of today's BMR/CMR examinations.

It is no secret that the future of UHF-BMR/CMR will not end at 7.0 T and that the field is moving apace into this direction. On the MR physics side the field strives to extend activities designed to master MR electrodynamics at fields of $B_0 \geq 7.0$ T by progressing numerical simulations. The first pioneering reports on EMF simulations dealing with B_1^+, SAR and temperature distribution for CMR at 10.5 T, 11.7 T or even 14.0 T have been outlined in this review or were released recently (201). On the experimental side, the recent progress in probing the local concentrations of fluorine, sodium, potassium and chlorine at 7.0 T provide convincing reasons for wide bore magnets with $B_0 \geq 7.0$ T, which spurred the installation of a 10.5 T whole-body MR system suitable for cardiac and body imaging (201). Alongside this progress there is intriguing news on potential future developments outlined in a report of the National Research Council dealing with high magnetic field science and its application (202). This report forwarded a call for a 20.0 T wide bore MR system, a technical development inspired by the recent progress at 7.0 T and by the early experience with small animal MR at 21.1 T (203) as well as by the lessons learned from the design and safety evaluation of superconducting 13.0 T magnet outserts with a 50 cm bore size retrofitted with a 12.0 T resistive insert to form a 25.0 T hybrid magnet tailored for structure research (204). Arguably, ^{1}H MR at 20.0 T might be elusive in the first run. Yet, the frequencies of X-nuclei at 20.0 T are below the ^{1}H resonance frequency at 7.0 T, with the exception of ^{31}P and ^{19}F. This makes technologies established for ^{1}H MR at 7.0 T ideal candidates to be perfected and fine-tuned for hetero-nuclear BMR/CMR at 20.0 T. For example, the sensitivity gain at 20.0 T is expected to reduce scan times for ^{31}P and ^{23} Na by a factor of eight versus today's 7.0 T capabilities. While this is, for the moment, merely a vision, it promises sodium MR with a sub-millimeter spatial resolution in 5–10 min scan time, and offers the potential for probing the heart with ^{31}P spectroscopy in clinically acceptable scan times versus today's groundbreaking studies using scan durations of approximately 2 h. Also, recognizing the pace and momentum of UHF-MR, the MR vendors have committed to no U-turn on the tesla road. In fact they are now driving with full throttle to set up the next generation of whole body 7.0 T magnets. Thitherto UHF-BMR/CMR techniques remain in a state of creative flux, and productive engagement in this area continues to drive further developments.

Acknowledgements

The authors wish to acknowledge the members of the Berlin Ultrahigh Field Facility (BUFF), Berlin, Germany; the members of the MR group at the Medical Metrology Department, Physikalisch-Technische Bundesanstalt, Berlin, Germany; the Working Group for Cardiac Magnetic Resonance, Charité, Berlin, Germany; Sebastian Aussenhofer, C. J. Gorter Center for High Field Magnetic Resonance, Leiden University Medical Center, Leiden, and Maurice M. Bizino and Hildo Lamb, Department of Radiology, Leiden University Medical Center, Leiden, The Netherlands; Stefan Haneder, Institute of Clinical Radiology and Nuclear Medicine, University Medical Center Mannheim, Heidelberg University, Heidelberg, Germany; Alexander Raaijmakers, Department of Radiotherapy, University Medical Centre Utrecht, Utrecht, The Netherlands; Matthew D. Robson and Christopher Rodgers, Radcliffe Department of Medicine, University of Oxford, Oxford, UK; Tom W. J. Scheenen, Department of Radiology, Radboud University Medical Centre, Nijmegen, The Netherlands; Lale Umutlu, Mark E. Ladd, Stefan Maderwald and Oliver Kraff, Erwin L. Hahn Institute, University Duisburg-Essen, Essen, Germany; Thea Marie Niendorf and Anna Tabea Niendorf, Aachen, Germany, who kindly contributed examples of their pioneering work or other valuable assistance. This work was supported (in part, C.O.) by the DZHK (German Centre for Cardiovascular Research) and by the BMBF (Federal Ministry of Education and Research). This work was funded (in part, A.G.) by the Helmholtz Alliance ICEMED – Imaging and Curing Environmental Metabolic Diseases, through the Initiative and Network Fund of the Helmholtz Association (ICEMED-Project 1210251). L.W. and H.W. received support by the BMBF (Federal Ministry of Education and Research, "KMU-innovativ": Medizintechnik MED-373-046).

REFERENCES

1. van den Bergen B, Van den Berg CAT, Bartels LW, Lagendijk JJW. 7 T body MRI: B_1 shimming with simultaneous SAR reduction. Phys. Med. Biol. 2007; 52: 5429.
2. Metzger GJ, Snyder C, Akgun C, Vaughan T, Ugurbil K, Van de Moortele PF. Local B_1^+ shimming for prostate imaging with transceiver arrays at 7T based on subject-dependent transmit phase measurements. Magn. Reson. Med. 2008; 59(2): 396–409.
3. van den Bergen B, van den Berg CA, Klomp DW, Lagendijk JJ. SAR and power implications of different RF shimming strategies in the pelvis for 7T MRI. J. Magn. Reson. Imaging 2009; 30(1): 194–202.
4. Umutlu L, Kraff O, Orzada S, Fischer A, Kinner S, Maderwald S, Antoch G, Quick HH, Forsting M, Ladd ME, Lauenstein TC. Dynamic contrast-enhanced renal MRI at 7 Tesla: preliminary results. Invest. Radiol. 2011; 46(7): 425–433.
5. Umutlu L, Orzada S, Kinner S, Maderwald S, Brote I, Bitz AK, Kraff O, Ladd SC, Antoch G, Ladd ME, Quick HH, Lauenstein TC. Renal imaging at 7 Tesla: preliminary results. Eur. Radiol. 2011; 21(4): 841–849.
6. van den Bergen B, Klomp DW, Raaijmakers AJ, de Castro CA, Boer VO, Kroeze H, Luijten PR, Lagendijk JJ, van den Berg CA. Uniform prostate imaging and spectroscopy at 7 T: comparison between a microstrip array and an endorectal coil. NMR Biomed. 2011; 24(4): 358–365.
7. Umutlu L, Maderwald S, Kraff O, Kinner S, Schaefer LC, Wrede K, Antoch G, Forsting M, Ladd ME, Lauenstein TC, Quick HH. New look at renal vasculature: 7 tesla nonenhanced T1-weighted FLASH imaging. J. Magn. Reson. Imaging 2012; 36(3): 714–721.
8. Snyder CJ, Delabarre L, Moeller S, Tian J, Akgun C, Van de Moortele PF, Bolan PJ, Ugurbil K, Vaughan JT, Metzger GJ. Comparison between eight- and sixteen-channel TEM transceive arrays for body imaging at 7 T. Magn. Reson. Med. 2012; 67(4): 954–964.
9. Arteaga de Castro CS, van den Bergen B, Luijten PR, van der Heide UA, van Vulpen M, Klomp DW. Improving SNR and B1 transmit field for an endorectal coil in 7 T MRI and MRS of prostate cancer. Magn. Reson. Med. 2012; 68(1): 311–318.
10. Kobus T, Bitz AK, van Uden MJ, Lagemaat MW, Rothgang E, Orzada S, Heerschap A, Scheenen TW. In vivo ^{31}P MR spectroscopic imaging of the human prostate at 7 T: safety and feasibility. Magn. Reson. Med. 2012; 68(6): 1683–1695.
11. Umutlu L, Maderwald S, Kinner S, Kraff O, Bitz AK, Orzada S, Johst S, Wrede K, Forsting M, Ladd ME, Lauenstein TC, Quick HH. First-pass contrast-enhanced renal MRA at 7 Tesla: initial results. Eur. Radiol. 2013; 23(4): 1059–1066.
12. Metzger GJ, Auerbach EJ, Akgun C, Simonson J, Bi X, Ugurbil K, van de Moortele PF. Dynamically applied B_1^+ shimming solutions for non-contrast enhanced renal angiography at 7.0 tesla. Magn. Reson. Med. 2013; 69(1): 114–126.
13. Luttje MP, Italiaander MG, Arteaga de Castro CS, van der Kemp WJ, Luijten PR, van Vulpen M, van der Heide UA, Klomp DW. ^{31}P MR spectroscopic imaging combined with ^{1}H MR spectroscopic imaging in the human prostate using a double tuned endorectal coil at 7T. Magn. Reson. Med. 2014; 72(6): 1516–1521.

14. Umutlu L, Kraff O, Fischer A, Kinner S, Maderwald S, Nassenstein K, Nensa F, Gruneisen J, Orzada S, Bitz AK, Forsting M, Ladd ME, Lauenstein TC. Seven-Tesla MRI of the female pelvis. Eur. Radiol. 2013; 23(9): 2364–2373.
15. Wu X, Schmitter S, Auerbach EJ, Ugurbil K, Van de Moortele PF. Mitigating transmit B_1 inhomogeneity in the liver at 7T using multi-spoke parallel transmit RF pulse design. Quant. Imaging Med. Surg. 2014; 4(1): 4–10.
16. Vos EK, Lagemaat MW, Barentsz JO, Futterer JJ, Zamecnik P, Roozen H, Orzada S, Bitz AK, Maas MC, Scheenen TW. Image quality and cancer visibility of T2-weighted magnetic resonance imaging of the prostate at 7 Tesla. Eur. Radiol. 2014; 24(8): 1950–1958.
17. Maas MC, Vos EK, Lagemaat MW, Bitz AK, Orzada S, Kobus T, Kraff O, Maderwald S, Ladd ME, Scheenen TW. Feasibility of T2-weighted turbo spin echo imaging of the human prostate at 7 tesla. Magn. Reson. Med. 2014; 71(5): 1711–1719.
18. Johst S, Orzada S, Fischer A, Umutlu L, Ladd ME, Maderwald S. Comparison of fat saturation techniques for single-shot fast spin echo sequences for 7-T body imaging. Invest. Radiol. 2014; 49(2): 101–108.
19. Fischer A, Kraff O, Orzada S, Nensa F, Schafer LC, Ladd ME, Umutlu L, Lauenstein TC. Ultrahigh-field imaging of the biliary tract at 7 T: initial results of gadoxetic acid-enhanced magnetic resonance cholangiography. Invest. Radiol. 2014; 49(5): 346–353.
20. Haneder S, Juras V, Michaely HJ, Deligianni X, Bieri O, Schoenberg SO, Trattnig S, Zbyn S. In vivo sodium (^{23}Na) imaging of the human kidneys at 7 T: preliminary results. Eur. Radiol. 2014; 24(2): 494–501.
21. Fischer A, Kraff O, Maderwald S, Beiderwellen K, Ladd ME, Forsting M, Lauenstein TC, Umutlu L. Non-enhanced T1-weighted liver vessel imaging at 7 Tesla. PLoS One 2014; 9(6): e97465.
22. Lagemaat MW, Vos EK, Maas MC, Bitz AK, Orzada S, van Uden MJ, Kobus T, Heerschap A, Scheenen TW. Phosphorus magnetic resonance spectroscopic imaging at 7 T in patients with prostate cancer. Invest. Radiol. 2014; 49(5): 363–372.
23. Lagemaat MW, Maas MC, Vos EK, Bitz AK, Orzada S, Weiland E, van Uden MJ, Kobus T, Heerschap A, Scheenen TW. ^{31}P MR spectroscopic imaging of the human prostate at 7 T: T_1 relaxation times, Nuclear Overhauser Effect, and spectral characterization. Magn. Reson. Med. 2014. DOI: 10.1002/mrm.25209
24. Kraff O, Fischer A, Nagel AM, Monninghoff C, Ladd ME. MRI at 7 tesla and above: demonstrated and potential capabilities. J. Magn. Reson. Imaging 2015; 41(1): 13–33.
25. Vaughan JT, Snyder CJ, DelaBarre LJ, Bolan PJ, Tian J, Bolinger L, Adriany G, Andersen P, Strupp J, Ugurbil K. Whole-body imaging at 7T: preliminary results. Magn. Reson. Med. 2009; 61(1): 244–248.
26. Snyder CJ, DelaBarre L, Metzger GJ, van de Moortele PF, Akgun C, Ugurbil K, Vaughan JT. Initial results of cardiac imaging at 7 Tesla. Magn. Reson. Med. 2009; 61(3): 517–524.
27. Frauenrath T, Hezel F, Heinrichs U, Kozerke S, Utting JF, Kob M, Butenweg C, Boesiger P, Niendorf T. Feasibility of cardiac gating free of interference with electro-magnetic fields at 1.5 Tesla, 3.0 Tesla and 7.0 Tesla using an MR-stethoscope. Invest. Radiol. 2009; 44(9): 539–547.
28. Brandts A, Westenberg JJ, Versluis MJ, Kroft LJ, Smith NB, Webb AG, de Roos A. Quantitative assessment of left ventricular function in humans at 7 T. Magn. Reson. Med. 2010; 64(5): 1471–1477.
29. van Elderen SG, Versluis MJ, Webb AG, Westenberg JJ, Doornbos J, Smith NB, de Roos A, Stuber M. Initial results on in vivo human coronary MR angiography at 7 T. Magn. Reson. Med. 2009; 62(6): 1379–1384.
30. van Elderen SG, Versluis MJ, Westenberg JJ, Agarwal H, Smith NB, Stuber M, de Roos A, Webb AG. Right coronary MR angiography at 7 T: a direct quantitative and qualitative comparison with 3 T in young healthy volunteers. Radiology 2010; 257(1): 254–259.
31. Versluis MJ, Tsekos N, Smith NB, Webb AG. Simple RF design for human functional and morphological cardiac imaging at 7tesla. J. Magn. Reson. 2009; 200(1): 161–166.
32. Niendorf T, Sodickson DK, Krombach GA, Schulz-Menger J. Toward cardiovascular MRI at 7 T: clinical needs, technical solutions and research promises. Eur. Radiol. 2010; 20(12): 2806–2816.
33. Frauenrath T, Hezel F, Renz W, d'Orth Tde G, Dieringer M, von Knobelsdorff-Brenkenhoff F, Prothmann M, Schulz Menger J, Niendorf T. Acoustic cardiac triggering: a practical solution for synchronization and gating of cardiovascular magnetic resonance at 7 Tesla. J. Cardiovasc. Magn. Reson. 2010; 12: 67.
34. von Knobelsdorff-Brenkenhoff F, Frauenrath T, Prothmann M, Dieringer MA, Hezel F, Renz W, Kretschel K, Niendorf T, Schulz-Menger J. Cardiac chamber quantification using magnetic resonance imaging at 7 Tesla – a pilot study. Eur. Radiol. 2010; 20(12): 2844–2852.
35. Dieringer MA, Renz W, Lindel T, Seifert F, Frauenrath T, von Knobelsdorff-Brenkenhoff F, Waiczies H, Hoffmann W, Rieger J, Pfeiffer H, Ittermann B, Schulz-Menger J, Niendorf T. Design and application of a four-channel transmit/receive surface coil for functional cardiac imaging at 7T. J. Magn. Reson. Imaging 2011; 33(3): 736–741.
36. Suttie JJ, Delabarre L, Pitcher A, van de Moortele PF, Dass S, Snyder CJ, Francis JM, Metzger GJ, Weale P, Ugurbil K, Neubauer S, Robson M, Vaughan T. 7 Tesla (T) human cardiovascular magnetic resonance imaging using FLASH and SSFP to assess cardiac function: validation against 1.5 T and 3 T. NMR Biomed. 2012; 25(1): 27–34.
37. Grassl A, Winter L, Thalhammer C, Renz W, Kellman P, Martin C, von Knobelsdorff-Brenkenhoff F, Tkachenko V, Schulz-Menger J, Niendorf T. Design, evaluation and application of an eight channel transmit/receive coil array for cardiac MRI at 7.0 T. Eur. J. Radiol. 2013; 82(5): 752–759.
38. Winter L, Kellman P, Renz W, Grassl A, Hezel F, Thalhammer C, von Knobelsdorff-Brenkenhoff F, Tkachenko V, Schulz-Menger J, Niendorf T. Comparison of three multichannel transmit/receive radiofrequency coil configurations for anatomic and functional cardiac MRI at 7.0T: implications for clinical imaging. Eur. Radiol. 2012; 22(10): 2211–2220.
39. Thalhammer C, Renz W, Winter L, Hezel F, Rieger J, Pfeiffer H, Graessl A, Seifert F, Hoffmann W, von Knobelsdorff-Brenkenhoff F, Tkachenko V, Schulz-Menger J, Kellman P, Niendorf T. Two-dimensional sixteen channel transmit/receive coil array for cardiac MRI at 7.0 T: design, evaluation, and application. J. Magn. Reson. Imaging 2012; 36(4): 847–857.
40. Frauenrath T, Fuchs K, Dieringer MA, Ozerdem C, Patel N, Renz W, Greiser A, Elgeti T, Niendorf T. Detailing the use of magnetohydrodynamic effects for synchronization of MRI with the cardiac cycle: a feasibility study. J. Magn. Reson. Imaging 2012; 36(2): 364–372.
41. Santoro D, Winter L, Muller A, Vogt J, Renz W, Ozerdem C, Grassl A, Tkachenko V, Schulz-Menger J, Niendorf T. Detailing radio frequency heating induced by coronary stents: a 7.0 Tesla magnetic resonance study. PLoS One 2012; 7(11): e49963.
42. Hezel F, Thalhammer C, Waiczies S, Schulz-Menger J, Niendorf T. High spatial resolution and temporally resolved T_2* mapping of normal human myocardium at 7.0 tesla: an ultrahigh field magnetic resonance feasibility study. PLoS One 2012; 7(12): e52324.
43. Niendorf T, Graessl A, Thalhammer C, Dieringer MA, Kraus O, Santoro D, Fuchs K, Hezel F, Waiczies S, Ittermann B, Winter L. Progress and promises of human cardiac magnetic resonance at ultrahigh fields: a physics perspective. J. Magn. Reson. 2013; 229: 208–222.
44. von Knobelsdorff-Brenkenhoff F, Tkachenko V, Winter L, Rieger J, Thalhammer C, Hezel F, Graessl A, Dieringer MA, Niendorf T, Schulz-Menger J. Assessment of the right ventricle with cardiovascular magnetic resonance at 7 Tesla. J. Cardiovasc. Magn. Reson. 2013; 15: 23.
45. Niendorf T, Schulz-Menger J. Cardiovascular ultrahigh field magnetic resonance imaging: challenges, technical solutions and opportunities. Radiologe 2013; 53(5): 422–428.
46. Winter L, Ozerdem C, Hoffmann W, Santoro D, Muller A, Waiczies H, Seemann R, Graessl A, Wust P, Niendorf T. Design and evaluation of a hybrid radiofrequency applicator for magnetic resonance imaging and rf induced hyperthermia: electromagnetic field simulations up to 14.0 tesla and proof-of-concept at 7.0 tesla. PLoS One 2013; 8(4): e61661.
47. Rodgers CT, Piechnik SK, Delabarre LJ, Van de Moortele PF, Snyder CJ, Neubauer S, Robson MD, Vaughan JT. Inversion recovery at 7 T in the human myocardium: measurement of T_1, inversion efficiency and B_1^+. Magn. Reson. Med. 2013; 70(4): 1038–1046.
48. Meloni A, Hezel F, Positano V, Keilberg P, Pepe A, Lombardi M, Niendorf T. Detailing magnetic field strength dependence and segmental artifact distribution of myocardial effective transverse relaxation rate at 1.5, 3.0, and 7.0 T. Magn. Reson. Med. 2014; 71(6): 2224–2230.
49. Schmitter S, DelaBarre L, Wu X, Greiser A, Wang D, Auerbach EJ, Vaughan JT, Ugurbil K, Van de Moortele PF. Cardiac imaging at 7 Tesla: single- and two-spoke radiofrequency pulse design with 16-channel parallel excitation. Magn. Reson. Med. 2013; 70(5): 1210–1219.

50. Bizino MB, Bonetti C, van der Geest RJ, Versluis MJ, Webb AG, Lamb HJ. High spatial resolution coronary magnetic resonance angiography at 7 T: comparison with low spatial resolution bright blood imaging. Invest. Radiol. 2014; 49(5): 326–330.
51. Tao Y, Hess AT, Keith GA, Rodgers CT, Liu A, Francis JM, Neubauer S, Robson MD. Optimized saturation pulse train for human first-pass myocardial perfusion imaging at 7T. Magn. Reson. Med. 2014. DOI: 10.1002/mrm.25262
52. Rodgers CT, Clarke WT, Snyder C, Vaughan JT, Neubauer S, Robson MD. Human cardiac ^{31}P magnetic resonance spectroscopy at 7 tesla. Magn. Reson. Med. 2014; 72(2): 304–315.
53. Graessl A, Renz W, Hezel F, Dieringer MA, Winter L, Oezerdem C, Rieger J, Kellman P, Santoro D, Lindel TD, Frauenrath T, Pfeiffer H, Niendorf T. Modular 32-channel transceiver coil array for cardiac MRI at 7.0T. Magn. Reson. Med. 2014; 72(1): 276–290.
54. Keith GA, Rodgers CT, Hess AT, Snyder CJ, Vaughan JT, Robson MD. Automated tuning of an eight-channel cardiac tranceive array at 7 Tesla using piezoelectric actuators. Magn. Reson. Med. 2014. DOI: 10.1002/mrm.25356
55. Aussenhofer SA, Webb AG. An eight-channel transmit/receive array of TE_{01} mode high permittivity ceramic resonators for human imaging at 7 T. J. Magn. Reson. 2014; 243: 122–129.
56. Hess AT, Bissell MM, Ntusi NA, Lewis AJ, Tunnicliffe EM, Greiser A, Stalder AF, Francis JM, Myerson SG, Neubauer S, Robson MD. Aortic 4D flow: quantification of signal-to-noise ratio as a function of field strength and contrast enhancement for 1.5T, 3T, and 7T. Magn. Reson. Med. 2014. DOI: 10.1002/mrm.25317
57. Winter L, Oberacker E, Özerdem C, Ji Y, von Knobelsdorff-Brenkenhoff F, Weidemann G, Ittermann B, Seifert F, Niendorf T. On the RF heating of intracoronary stents at 7.0 T. Magn. Reson. Med. 2014. DOI: 10.1002/mrm.25483
58. Schmitter S, Wu X, Ugurbil K, Van de Moortele PF. Design of parallel transmission radiofrequency pulses robust against respiration in cardiac MRI at 7 Tesla. Magn. Reson. Med. 2014. DOI: 10.1002/mrm.25512
59. Klix S, Els A, Paul K, Graessl A, Oezerdem C, Weinberger O, Winter L, Thalhammer C, Huelnhagen T, Rieger J, Mehling H, Schulz Menger J, Niendorf T. On the subjective acceptance during cardiovascular magnetic resonance imaging at 7.0 tesla. PLoS One 2015 Jan 26; 10(1): e0117095. DOI: 10.1371/journal.pone.0117095. eCollection 2015
60. Adriany G, Ritter J, Vaughan JT, Ugurbil K, Moortele PF. Experimental verification of enhanced B1 shim performance with a Z-encoding RF coil array at 7 tesla. In *Proceedings of the Joint Annual Meeting of ISMRM-ESMRMB, Stockholm, Sweden*. The International Society of Magnetic Resonance in Medicine, Berkeley, California, USA, 2010; 3831.
61. Maderwald S, Orzada S, Schaefer LC, Bitz AK, Brote I, Kraff O, Theysohn JM, Ladd ME, Ladd SC, Quick HH. 7T human in vivo cardiac imaging with an 8-channel transmit/receive array. In *Proceedings of the 17th Annual Meeting of ISMRM*. The International Society of Magnetic Resonance in Medicine, Berkeley, California, USA, 2009; 822.
62. Ipek O, Raaijmakers AJ, Klomp DW, Lagendijk JJ, Luijten PR, van den Berg CA. Characterization of transceive surface element designs for 7 tesla magnetic resonance imaging of the prostate: radiative antenna and microstrip. Phys. Med. Biol. 2012; 57(2): 343–355.
63. Raaijmakers AJ, Ipek O, Klomp DW, Possanzini C, Harvey PR, Lagendijk JJ, van den Berg CA. Design of a radiative surface coil array element at 7 T: the single-side adapted dipole antenna. Magn. Reson. Med. 2011; 66(5): 1488–1497.
64. Özerdem C, Winter L, Hoffmann W, Waiczies H, Seeman R, Santoro D, Müller A, Ok A, Lindel T, Ittermann B, Niendorf T. Design and evaluation of a dipole antenna TX/RX element as a building block for combined MR imaging and RF hyperthermia at 7.0 T. In *Proceedings of the 20th Annual Meeting of ISMRM, Melbourne, Victoria, Australia*. The International Society of Magnetic Resonance in Medicine, Berkeley, California, USA, 2012; 2641.
65. Ipek O, Raaijmakers AJ, Lagendijk JJ, Luijten PR, van den Berg CA. Intersubject local SAR variation for 7T prostate MR imaging with an eight-channel single-side adapted dipole antenna array. Magn. Reson. Med. 2014; 71(4): 1559–1567.
66. Raaijmakers AJE, El Aidi H, Versluis M, Webb AG, Lamb HJ, Luijten PR, van den Berg CAT, Leiner T. Comprehensive coronary artery imaging at 7.0 T: proof of feasibility. In *Proceedings of the Joint Annual Meeting ISMRM-ESMRMB, Milan, Italy*. The International Society of Magnetic Resonance in Medicine, Berkeley, California, USA, 2014; 4923.
67. Raaijmakers AJE, Voogt I, Klomp DWJ, Luijten PR, van den Berg CAT. Dipole antenna without ceramic substrate and still low SAR: the fractionated dipole antenna. In *Proceedings of the 21th Annual Meeting of ISMRM, Salt Lake City, Utah, USA*. The International Society of Magnetic Resonance in Medicine, Berkeley, California, USA, 2013; 4382.
68. Chen G, Cloos M, Sodickson DK, Wiggins GC. A 7T 8 channel transmit-receive dipole array for head imaging: dipole element and coil evaluation. In *Proceedings of the Joint Annual Meeting of ISMRM-ESMRMB, Milan, Italy*. The International Society of Magnetic Resonance in Medicine, Berkeley, California, USA, 2014; 621.
69. Chen G, Cloos M, Lattanzi R, Sodickson DK, Wiggins GC. Bent electric dipoles: a novel coil design inspired by the ideal current pattern for central SNR at 7 tesla. Proc. Int. Soc. Magh. Reson. Med. 2014; 22: 402.
70. Lakshmanan K, Cloos M, Lattanzi R, Sodickson DK, Novivkov D, Wiggins GC. The circular dipole. In *Proceedings of the Joint Meeting ISMRM-ESMRMB, Milan, Italy*. The International Society of Magnetic Resonance in Medicine, Berkeley, California, USA, 2014; 315.
71. Lee W, Sodickson DK, Wiggins GC. A new UHF transceiver antenna design: modified folded dipole. In *Proceedings of the 21th Annual Meeting of ISMRM, Salt Lake City, Utah, USA*. The International Society of Magnetic Resonance in Medicine, Berkeley, California, USA, 2013; 4367.
72. Lattanzi R, Sodickson DK. Ideal current patterns yielding optimal signal-to-noise ratio and specific absorption rate in magnetic resonance imaging: computational methods and physical insights. Magn. Reson. Med. 2012; 68(1): 286–304.
73. Wiggins GJ, Zhang B, Lattanzi R, Chen GM, Sodickson DK. The electric dipole array: an attempt to match the ideal current pattern for central SNR at 7 tesla. In *Proceedings of the 20th Annual Meeting of ISMRM, Melbourne, Victoria, Australia*. The International Society of Magnetic Resonance in Medicine, Berkeley, California, USA, 2012; 541.
74. Akoka S, Franconi F, Seguin F, Le Pape A. Radiofrequency map of an NMR coil by imaging. Magn. Reson. Imaging 1993; 11(3): 437–441.
75. Cunningham CH, Pauly JM, Nayak KS. Saturated double-angle method for rapid B_1+ mapping. Magn. Reson. Med. 2006; 55(6): 1326–1333.
76. Insko EK, Bolinger L. Mapping of the radiofrequency field. J. Magn. Reson. A 1993; 103: 83–85.
77. Stollberger R, Wach P. Imaging of the active B_1 field *in vivo*. Magn. Reson. Med. 1996; 35(2): 246–251.
78. Klose U. Mapping of the radio frequency magnetic field with a MR snapshot FLASH technique. Med. Phys. 1992; 19(4): 1099–1104.
79. Yarnykh VL. Actual flip-angle imaging in the pulsed steady state: a method for rapid three-dimensional mapping of the transmitted radiofrequency field. Magn. Reson. Med. 2007; 57(1): 192–200.
80. Dowell NG, Tofts PS. Fast, accurate, and precise mapping of the RF field in vivo using the 180 degrees signal null. Magn. Reson. Med. 2007; 58(3): 622–630.
81. Stanisz GJ, Odrobina EE, Pun J, Escaravage M, Graham SJ, Bronskill MJ, Henkelman RM. T_1, T_2 relaxation and magnetization transfer in tissue at 3T. Magn. Reson. Med. 2005; 54(3): 507–512.
82. Nehrke K, Bornert P. DREAM – a novel approach for robust, ultrafast, multislice B_1 mapping. Magn. Reson. Med. 2012; 68(5): 1517–1526.
83. Linz P, Santoro D, Renz W, Rieger J, Ruehle A, Ruff J, Deimling M, Rakova N, Muller DN, Luft FC, Titze J, Niendorf T. Skin sodium measured with ^{23}Na MRI at 7.0 T. NMR Biomed. 2015; 28(1): 54–62.
84. Nehrke K, Sprinkart AM, Bornert P. An in vivo comparison of the DREAM sequence with current RF shim technology. Magn. Reson. Mater. Phys. Biol. Med. 2014. DOI: 10.1007/s10334-014-0454-3
85. Boernert P, Nehrke K, Wang J. Magnetization prepared DREAM for fast flow-robust B1+ mapping. In *Proceedings of theJoint Meeting of ISMRM-ESMRMB, Milan, Italy*. The International Society of Magnetic Resonance in Medicine, Berkeley, California, USA, 2014; 4383.
86. Morrell GR, Schabel MC. An analysis of the accuracy of magnetic resonance flip angle measurement methods. Phys. Med. Biol. 2010; 55(20): 6157–6174.
87. Morrell GR. A phase-sensitive method of flip angle mapping. Magn. Reson. Med. 2008; 60(4): 889–894.
88. Mugler JPI, Miller GW, Altes TA, de Lange EE, Brookeman JR. A low-flip-angle, phase-based method for accurately calibrating the

transmitter in hyperpolarized-gas MRI. In *Proceedings of the 13th Annual Meeting of ISMRM, Miami Beach, USA*. The International Society of Magnetic Resonance in Medicine, Berkeley, California, USA, 2005; 789.
89. Santoro D, Rivoire J, Meise F, Terekhov M, Salhi Z, Gast K, Schreiber LM. Three-dimensional mapping of the B_1 field using an optimized phase-based method: application to hyperpolarized ^{3}He in lungs. Magn. Reson. Med. 2011; 65(4): 1166–1172.
90. Santoro D, von Samson-Himmelstjerna F, Carinci F, Hezel F, Dieringer M, Niendorf T. Cardiac triggered B_1^+ mapping using Bloch Siegert in the heart at 3T. In *Proceedings of the 20th Annual Meeting of ISMRM, Melbourne, Victoria, Australia*. The International Society of Magnetic Resonance in Medicine, Berkeley, California, USA, 2012; 3840.
91. Sacolick LI, Wiesinger F, Hancu I, Vogel MW. B_1 mapping by Bloch–Siegert shift. Magn. Reson. Med. 2010; 63(5): 1315–1322.
92. Curtis AT, Gilbert KM, Klassen LM, Gati JS, Menon RS. Slice-by-slice B1+ shimming at 7 T. Magn. Reson. Med. 2012; 68(4): 1109–1116.
93. Carinci F, Santoro D, von Samson-Himmelstjerna F, Lindel TD, Dieringer MA, Niendorf T. Characterization of phase-based methods used for transmission field uniformity mapping: a magnetic resonance study at 3.0 T and 7.0 T. PLoS One 2013; 8(3): e57982.
94. Nehrke K, Versluis MJ, Webb A, Bornert P. Volumetric B_1^+ mapping of the brain at 7T using DREAM. Magn. Reson. Med. 2014; 71(1): 246–256.
95. Bitz AK, Brote I, Orzada S, Kraff O, Maderwald S, Quick HH, Solbach K, Bahr A, Fautz H-P, Schmitt F, Ladd ME. Comparison of simulation-based and measurement-based RF shimming for whole-body MRI at 7 Tesla. In *Proceedings of the Joint Annual Meeting of ISMRM–ESMRMB, Stockholm, Sweden*. The International Society of Magnetic Resonance in Medicine, Berkeley, California, USA, 2010; 4720.
96. Christ A, Kainz W, Hahn EG, Honegger K, Zefferer M, Neufeld E, Rascher W, Janka R, Bautz W, Chen J. The Virtual Family – development of surface-based anatomical models of two adults and two children for dosimetric simulations. Phys. Med. Biol. 2010; 55: N23.
97. Orzada S, Maderwald S, Poser BA, Bitz AK, Quick HH, Ladd ME. RF excitation using time interleaved acquisition of modes (TIAMO) to address B_1 inhomogeneity in high-field MRI. Magn. Reson. Med. 2010; 64(2): 327–333.
98. Orzada S, Johst S, Maderwald S, Bitz AK, Solbach K, Ladd ME. Mitigation of $B1^+$ inhomogeneity on single-channel transmit systems with TIAMO. Magn. Reson. Med. 2013; 70(1): 290–294.
99. Lindel T, Greiser A, Waxmann P, Dietterle M, Seifert F, Fontius U, Renz W, Dieringer MA, Frauenrath T, Schulz-Menger J, Niendorf T, Ittermann B. Cardiac CINE MRI at 7 T using a transmit array. In *Proceedings of the 20th Annual Meeting of ISMRM, Melbourne, Victoria, Australia*. The International Society of Magnetic Resonance in Medicine, Berkeley, California, USA, 2012; 1227.
100. Metzger G, Bi X, DelaBarre L, Shah S, Ugurbil K, van de Moortele P-F, Vaughan T, Zuehlsdorff S. Left coronary artery imaging at 7T: initial results using multiple B1+ shimming algorithms and targets. In *Proceedings of the 21st Annual Meeting of ISMRM, Montreal, Quebec, Canada*. The International Society of Magnetic Resonance in Medicine, Berkeley, California, USA, 2011; 116.
101. Schmitter S, Schnell S, Ugurbil K, Markl M, van de Moortele PF. 4D Flow imaging in the aorta at 7T: impact of dynamic RF shimming and kt-acceleration. In *Proceedings of the Joint Annual Meeting of ISMRM-ESMRMB, Milan, Italy*. The International Society of Magnetic Resonance in Medicine, Berkeley, California, USA, 2014; 992.
102. Xiufeng L, Snyder CJ, van de Moortele P-F, Ugurbil K, Metzger GJ. Non-contrast enhanced human renal perfusion imaging using arterial spin labeling at 7T: initial experience. In *Proceedings of the 20th Annual Meeting of ISMRM, Melbourne, Victoria, Australia*. The International Society of Magnetic Resonance in Medicine, Berkeley, California, USA, 2012; 1310.
103. Setsompop K, Wald LL, Alagappan V, Gagoski BA, Adalsteinsson E. Magnitude least squares optimization for parallel radio frequency excitation design demonstrated at 7 Tesla with eight channels. Magn. Reson. Med. 2008; 59(4): 908–915.
104. Katscher U, Bornert P. Parallel RF transmission in MRI. NMR Biomed. 2006; 19(3): 393–400.
105. Katscher U, Bornert P, Leussler C, van den Brink JS. Transmit SENSE. Magn. Reson. Med. 2003; 49(1): 144–150.
106. Zhu Y. Parallel excitation with an array of transmit coils. Magn. Reson. Med. 2004; 51(4): 775–784.
107. Ullmann P, Junge S, Wick M, Seifert F, Ruhm W, Hennig J. Experimental analysis of parallel excitation using dedicated coil setups and simultaneous RF transmission on multiple channels. Magn. Reson. Med. 2005; 54(4): 994–1001.
108. Sharma A, Bammer R, Stenger VA, Grissom WA. Low peak power multiband spokes pulses for B_1^+ inhomogeneity-compensated simultaneous multislice excitation in high field MRI. Magn. Reson. Med. 2014. DOI: 10.1002/mrm.25455
109. Norris DG, Boyacioglu R, Schulz J, Barth M, Koopmans PJ. Application of PINS radiofrequency pulses to reduce power deposition in RARE/turbo spin echo imaging of the human head. Magn. Reson. Med. 2014; 71(1): 44–49.
110. Kramer CM, Barkhausen J, Flamm SD, Kim RJ, Nagel E. Standardized cardiovascular magnetic resonance imaging (CMR) protocols, Society for Cardiovascular Magnetic Resonance: Board of Trustees Task Force on Standardized Protocols. J. Cardiovasc. Magn. Reson. 2008; 10: 35.
111. Kramer CM, Barkhausen J, Flamm SD, Kim RJ, Nagel E. Standardized cardiovascular magnetic resonance (CMR) protocols 2013 update. J. Cardiovasc. Magn. Reson. 2013; 15: 91.
112. Wagenhaus B, Pohlmann A, Dieringer MA, Els A, Waiczies H, Waiczies S, Schulz-Menger J, Niendorf T. Functional and morphological cardiac magnetic resonance imaging of mice using a cryogenic quadrature radiofrequency coil. PLoS One 2012; 7(8): e42383.
113. Vitanis V, Manka R, Giese D, Pedersen H, Plein S, Boesiger P, Kozerke S. High resolution three-dimensional cardiac perfusion imaging using compartment-based k-t principal component analysis. Magn. Reson. Med. 2011; 65(2): 575–587.
114. Schar M, Vonken EJ, Stuber M. Simultaneous B_0- and B_1+—map acquisition for fast localized shim, frequency, and RF power determination in the heart at 3 T. Magn. Reson. Med. 2010; 63(2): 419–426.
115. Reeder SB, Faranesh AZ, Boxermann JL, McVeigh ER. In vivo measurement of T_2* and field inhomogeneity maps in the human heart at 1.5 T. Magn. Reson. Med. 1998; 39: 988–998.
116. O'Regan D, Callaghan M, Fitzpatrick J, Naoumova R, Hajnal J, Schmitz S. Cardiac T_2* and lipid measurement at 3.0 T – initial experience. Eur. Radiol. 2008; 18: 800–805.
117. Pepe A, Positano V, Santarelli MF, Sorrentino F, Cracolici E, De Marchi D, Maggio A, Midiri M, Landini L, Lombardi M. Multislice multiecho T2* cardiovascular magnetic resonance for detection of the heterogeneous distribution of myocardial iron overload. J. Magn. Reson. Imaging 2006; 23(5): 662–668.
118. Dharmakumar R, Arumana JM, Tang R, Harris K, Zhang Z, Li D. Assessment of regional myocardial oxygenation changes in the presence of coronary artery stenosis with balanced SSFP imaging at 3.0 T: theory and experimental evaluation in canines. J. Magn. Reson. Imaging 2008; 27(5): 1037–1045.
119. Duyn JH, van Gelderen P, Li TQ, de Zwart JA, Koretsky AP, Fukunaga M. High-field MRI of brain cortical substructure based on signal phase. Proc. Natl. Acad. Sci. U. S. A. 2007; 104(28): 11796–11801.
120. Lee J, van Gelderen P, Kuo LW, Merkle H, Silva AC, Duyn JH. T2*-based fiber orientation mapping. Neuroimage 2011; 57(1): 225–234.
121. Deistung A, Schafer A, Schweser F, Biedermann U, Turner R, Reichenbach JR. Toward *in vivo* histology: a comparison of quantitative susceptibility mapping (QSM) with magnitude-, phase-, and R_2*-imaging at ultra-high magnetic field strength. Neuroimage 2013; 65: 299–314.
122. Ogawa S, Menon RS, Tank DW, Kim SG, Merkle H, Ellermann JM, Ugurbil K. Functional brain mapping by blood oxygenation level-dependent contrast magnetic resonance imaging. A comparison of signal characteristics with a biophysical model. Biophys. J. 1993; 64(3): 803–812.
123. Ziener CH, Kampf T, Reents G, Schlemmer HP, Bauer WR. Spin dephasing in a magnetic dipole field. Phys. Rev. E 2012; 85(5 Pt 1): 051908.
124. Ziener CH, Kampf T, Melkus G, Jakob PM, Schlemmer HP, Bauer WR. Signal evolution in the local magnetic field of a capillary – analogy to the damped driven harmonic oscillator. Magn. Reson. Imaging 2012; 30(4): 540–553.
125. Hernando D, Vigen KK, Shimakawa A, Reeder SB. R_2 mapping in the presence of macroscopic B_0 field variations. Magn. Reson. Med. 2011; 68(3): 830–840.

126. Pohlmann A, Arakelyan K, Hentschel J, Cantow K, Flemming B, Ladwig M, Waiczies S, Seeliger E, Niendorf T. Detailing the relation between renal T2* and renal tissue pO2 using an integrated approach of parametric magnetic resonance imaging and invasive physiological measurements. Invest. Radiol. 2014; 49(8): 547–560.
127. Pohlmann A, Hentschel J, Fechner M, Hoff U, Bubalo G, Arakelyan K, Cantow K, Seeliger E, Flemming B, Waiczies H, Waiczies S, Schunck WH, Dragun D, Niendorf T. High temporal resolution parametric MRI monitoring of the initial ischemia/reperfusion phase in experimental acute kidney injury. PLoS One 2013; 8(2): e57411.
128. Messroghli DR, Radjenovic A, Kozerke S, Higgins DM, Sivananthan MU, Ridgway JP. Modified Look-Locker inversion recovery (MOLLI) for high-resolution T_1 mapping of the heart. Magn. Reson. Med. 2004; 52(1): 141–146.
129. von Knobelsdorff-Brenkenhoff F, Prothmann M, Dieringer MA, Wassmuth R, Greiser A, Schwenke C, Niendorf T, Schulz-Menger J. Myocardial T_1 and T_2 mapping at 3 T: reference values, influencing factors and implications. J. Cardiovasc. Magn. Reson. 2013; 15(1): 53.
130. Messroghli DR, Niendorf T, Schulz-Menger J, Dietz R, Friedrich MG. T_1 mapping in patients with acute myocardial infarction. J. Cardiovasc. Magn. Reson. 2003; 5(2): 353–359.
131. Piechnik SK, Ferreira VM, Dall'Armellina E, Cochlin LE, Greiser A, Neubauer S, Robson MD. Shortened Modified Look-Locker Inversion recovery (ShMOLLI) for clinical myocardial T1-mapping at 1.5 and 3 T within a 9 heartbeat breathhold. J. Cardiovasc. Magn. Reson. 2010; 12: 69.
132. Dieringer MA, Deimling M, Santoro D, Wuerfel J, Madai VI, Sobesky J, von Knobelsdorff-Brenkenhoff F, Schulz-Menger J, Niendorf T. Rapid parametric mapping of the longitudinal relaxation time t1 using two-dimensional variable flip angle magnetic resonance imaging at 1.5 tesla, 3 tesla, and 7 tesla. PLoS One 2014; 9(3): e91318.
133. Hernando D, Kellman P, Haldar JP, Liang ZP. Robust water/fat separation in the presence of large field inhomogeneities using a graph cut algorithm. Magn. Reson. Med. 2010; 63(1): 79–90.
134. Kellman P, Hezel F, Shah S, Renz W, Thalhammer C, Schulz Menger J, Niendorf T. Fat–water separated imaging at 7T: initial results for cardiac applications. In *Proceedings of the 19th Annual Meeting of ISMRM, Montreal, Quebec, Canada*. The International Society of Magnetic Resonance in Medicine, Berkeley, California, USA, 2011; 597.
135. Hezel F, Kellman P, Thalhammer C, Özerdem C, Renz W, Niendorf T. Initial results of abdominal MRI at 7T using a 16 channel transmit/receive coil. In *Proceedings of the 19th Annual Meeting of ISMRM, Montreal, Quebec, Canada*. The International Society of Magnetic Resonance in Medicine, Berkeley, California, USA, 2011; 595.
136. Hezel F, Graessl A, Kellman P, Niendorf T. Feasibility of abdominal MRI at 7.0 T using a novel 32 channel transceiver coil array. In *Proceedings of the 20th Annual Meeting of ISMRM, Melbourne, Victoria, Australia*. The International Society of Magnetic Resonance in Medicine, Berkeley, California, USA, 2012; 2808.
137. Niendorf T, Hardy CJ, Giaquinto RO, Gross P, Cline HE, Zhu Y, Kenwood G, Cohen S, Grant AK, Joshi S, Rofsky NM, Sodickson DK. Toward single breath-hold whole-heart coverage coronary MRA using highly accelerated parallel imaging with a 32-channel MR system. Magn. Reson. Med. 2006; 56(1): 167–176.
138. Niendorf T, Saranathan M, Lingamneni A, Pedrosa I, Spencer M, Cline H, Foo TK, Rofsky NM. Short breath-hold, volumetric coronary MR angiography employing steady-state free precession in conjunction with parallel imaging. Magn. Reson. Med. 2005; 53(4): 885–894.
139. Hagberg GE, Scheffler K. Effect of r_1 and r_2 relaxivity of gadolinium-based contrast agents on the T_1-weighted MR signal at increasing magnetic field strengths. Contrast Media Mol. Imaging 2013; 8(6): 456–465.
140. Kalavagunta C, Michaeli S, Metzger GJ. *In vitro* Gd-DTPA relaxometry studies in oxygenated venous human blood and aqueous solution at 3 and 7 T. Contrast Media Mol. Imaging 2014; 9(2): 169–176.
141. Fuchs K, Hezel F, Klix S, Mekle R, Wuerfel J, Niendorf T. Simultaneous dual contrast weighting using double echo rapid acquisition with relaxation enhancement (RARE) imaging. Magn. Reson. Med. 2014 Dec; 72(6): 1590–1598.
142. Klix S, Hezel F, Fuchs K, Ruff J, Dieringer MA, Niendorf T. Accelerated fast spin-echo magnetic resonance imaging of the heart using a self-calibrated split-echo approach. PLoS One 2014; 9(4): e94654.
143. Voit D, Zhang S, Unterberg-Buchwald C, Sohns JM, Lotz J, Frahm J. Real-time cardiovascular magnetic resonance at 1.5 T using balanced SSFP and 40 ms resolution. J. Cardiovasc. Magn. Reson. 2013; 15: 79.
144. Kowallick JT, Joseph AA, Unterberg-Buchwald C, Fasshauer M, van Wijk K, Merboldt KD, Voit D, Frahm J, Lotz J, Sohns JM. Real-time phase-contrast flow MRI of the ascending aorta and superior vena cava as a function of intrathoracic pressure (Valsalva manoeuvre). Br. J. Radiol. 2014; 87(1042): 20140401.
145. Fasshauer M, Joseph AA, Kowallick JT, Unterberg-Buchwald C, Merboldt KD, Voit D, Steinmetz M, Staab W, Schaetz S, Zhang S, Frahm J, Lotz J, Sohns JM. Real-time phase-contrast flow MRI of haemodynamic changes in the ascending aorta and superior vena cava during Mueller manoeuvre. Clin. Radiol. 2014; 69(10): 1066–1071.
146. Joseph A, Kowallick JT, Merboldt KD, Voit D, Schaetz S, Zhang S, Sohns JM, Lotz J, Frahm J. Real-time flow MRI of the aorta at a resolution of 40 msec. J. Magn. Reson. Imaging 2014; 40(1): 206–213.
147. Courtier J, Ohliger M, Rhee SJ, Terreblanche O, Heyman MB, MacKenzie JD. Shooting a moving target: use of real-time cine magnetic resonance imaging in assessment of the small bowel. J. Pediatr. Gastroenterol. Nutr. 2013; 57(4): 426–431.
148. Talasz H, Kremser C, Kofler M, Kalchschmid E, Lechleitner M, Rudisch A. Proof of concept: differential effects of Valsalva and straining maneuvers on the pelvic floor. Eur. J. Obstet. Gynecol. Reprod. Biol. 2012; 164(2): 227–233.
149. Arakelyan K, Cantow K, Hentschel J, Flemming B, Pohlmann A, Ladwig M, Niendorf T, Seeliger E. Early effects of an x-ray contrast medium on renal T_2*/T_2 MRI as compared to short-term hyperoxia, hypoxia and aortic occlusion in rats. Acta Physiol 2013; 208(2): 202–213.
150. Niendorf T, Pohlmann A, Arakelyan K, Flemming B, Cantow K, Hentschel J, Grosenick D, Ladwig M, Reimann H, Klix S, Waiczies S, Seeliger E. How bold is blood oxygenation level-dependent (BOLD) magnetic resonance imaging of the kidney? Opportunities, challenges and future directions. Acta Physiol 2015; 213(1): 19–38.
151. Cornud F, Delongchamps NB, Mozer P, Beuvon F, Schull A, Muradyan N, Peyromaure M. Value of multiparametric MRI in the work-up of prostate cancer. Curr. Urol. Rep. 2012; 13(1): 82–92.
152. Akin O, Sala E, Moskowitz CS, Kuroiwa K, Ishill NM, Pucar D, Scardino PT, Hricak H. Transition zone prostate cancers: features, detection, localization, and staging at endorectal MR imaging. Radiology 2006; 239(3): 784–792.
153. Sala E, Eberhardt SC, Akin O, Moskowitz CS, Onyebuchi CN, Kuroiwa K, Ishill N, Zelefsky MJ, Eastham JA, Hricak H. Endorectal MR imaging before salvage prostatectomy: tumor localization and staging. Radiology 2006; 238(1): 176–183.
154. Roethke M, Anastasiadis AG, Lichy M, Werner M, Wagner P, Kruck S, Claussen CD, Stenzl A, Schlemmer HP, Schilling D. MRI-guided prostate biopsy detects clinically significant cancer: analysis of a cohort of 100 patients after previous negative TRUS biopsy. World J. Urol. 2012; 30(2): 213–218.
155. Madelin G, Regatte RR. Biomedical applications of sodium MRI in vivo. J. Magn. Reson. Imaging 2013; 38(3): 511–529.
156. Sandstede JJW, Hillenbrand H, Beer M, Pabst T, Butter F, Machann W, Bauer W, Hahn D, Neubauer S. Time course of 23Na signal intensity after myocardial infarction in humans. Magn. Reson. Med. 2004; 52(3): 545–551.
157. Nagel AM, Laun FB, Weber MA, Matthies C, Semmler W, Schad LR. Sodium MRI using a density-adapted 3D radial acquisition technique. Magn. Reson. Med. 2009; 62(6): 1565–1573.
158. Resetar A, Hoffmann SH, Graessl A, Waiczies H, Niendorf T, Nagel A. Retrospectively gated CINE 23Na imaging of the heart at 7.0 T using density-adapted 3D projection reconstruction. In *Proceedings of the Joint Meeting of ISMRM-ESMRMB, Milan, Italy*. The International Society of Magnetic Resonance in Medicine, Berkeley, California, USA, 2014; 436.
159. Kopp C, Linz P, Wachsmuth L, Dahlmann A, Horbach T, Schofl C, Renz W, Santoro D, Niendorf T, Muller DN, Neininger M, Cavallaro A, Eckardt KU, Schmieder RE, Luft FC, Uder M, Titze J. ^{23}Na magnetic resonance imaging of tissue sodium. Hypertension 2012; 59(1): 167–172.
160. Gnahm C, Bock M, Bachert P, Semmler W, Behl NG, Nagel AM. Iterative 3D projection reconstruction of ^{23}Na data with an ^{1}H MRI constraint. Magn. Reson. Med. 2014; 71(5): 1720–1732.

161. Frauenrath T, Niendorf T, Kob M. Acoustic method for synchronization of magnetic resonance imaging (MRI). Acta Acust. Acust. 2008; 94(1): 148–155.
162. Becker M, Frauenrath T, Hezel F, Krombach GA, Kremer U, Koppers B, Butenweg C, Goemmel A, Utting JF, Schulz-Menger J, Niendorf T. Comparison of left ventricular function assessment using phonocardiogram- and electrocardiogram-triggered 2D SSFP CINE MR imaging at 1.5 T and 3.0 T. Eur. Radiol. 2010; 20(6): 1344–1355.
163. IEC. 60601-2-33 *Medical Electrical Equipment – Part 2–33: Particular Requirements for the Basic Safety and Essential Performance of Magnetic Resonance Equipment for Medical Diagnosis*. Edition 3.0. 2010.
164. Wang Z, Lin JC, Mao W, Liu W, Smith MB, Collins CM. SAR and temperature: simulations and comparison to regulatory limits for MRI. J. Magn. Reson. Imaging 2007; 26(2): 437–441.
165. Murbach M, Neufeld E, Capstick M, Kainz W, Brunner DO, Samaras T, Pruessmann KP, Kuster N. Thermal tissue damage model analyzed for different whole-body SAR and scan durations for standard MR body coils. Magn. Reson. Med. 2014; 71(1): 421–431.
166. Hoult DI. Sensitivity and power deposition in a high-field imaging experiment. J. Magn. Reson. Imaging 2000; 12(1): 46–67.
167. Collins CM, Smith MB. Calculations of B_1 distribution, SNR, and SAR for a surface coil adjacent to an anatomically-accurate human body model. Magn. Reson. Med. 2001; 45(4): 692–699.
168. Seifert F, Wubbeler G, Junge S, Ittermann B, Rinneberg H. Patient safety concept for multichannel transmit coils. J. Magn. Reson. Imaging 2007; 26(5): 1315–1321.
169. Lattanzi R, Sodickson D, Grant A, Zhu Y. Electrodynamic constraints on homogeneity and radiofrequency power deposition in multiple coil excitations. Magn. Reson. Med. 2009; 61(2): 315–334.
170. Zhu Y, Alon L, Deniz CM, Brown R, Sodickson DK. System and SAR characterization in parallel RF transmission. Magn. Reson. Med. 2011; 67(5): 1367–1378.
171. Graesslin I, Vernickel P, Bornert P, Nehrke K, Mens G, Harvey P, Katscher U. Comprehensive RF safety concept for parallel transmission MR. Magn. Reson. Med. 2014. DOI: 10.1002/mrm.25425
172. Wolf S, Diehl D, Gebhardt M, Mallow J, Speck O. SAR simulations for high-field MRI: how much detail, effort, and accuracy is needed? Magn. Reson. Med. 2012; 69(4): 1157–1168.
173. Eichfelder G, Gebhardt M. Local specific absorption rate control for parallel transmission by virtual observation points. Magn. Reson. Med. 2011; 66(5): 1468–1476.
174. Graesslin I, Homann H, Biederer S, Bornert P, Nehrke K, Vernickel P, Mens G, Harvey P, Katscher U. A specific absorption rate prediction concept for parallel transmission MR. Magn. Reson. Med. 2012; 68 (5): 1664–1674.
175. Homann H, Graesslin I, Eggers H, Nehrke K, Vernickel P, Katscher U, Dossel O, Bornert P. Local SAR management by RF shimming: a simulation study with multiple human body models. Magn. Reson. Mater. Phys. Biol. Med. 2012; 25(3): 193–204.
176. Homann H, Bornert P, Eggers H, Nehrke K, Dossel O, Graesslin I. Toward individualized SAR models and in vivo validation. Magn. Reson. Med. 2011; 66(6): 1767–1776.
177. Voigt T, Homann H, Katscher U, Doessel O. Patient-individual local SAR determination: in vivo measurements and numerical validation. Magn. Reson. Med. 2012; 68(4): 1117–1126.
178. Murbach M, Neufeld E, Pruessmann KP, Kuster N. Safe MR scan times based on CEM43 tissue damage thresholds, using electromagnetic and thermal simulations with anatomically correct human models and considering local thermoregulation. In *Proceedings of the 20th Annual Meeting of ISMRM, Melbourne, Victoria, Australia*. The International Society of Magnetic Resonance in Medicine, Berkeley, California, USA, 2012; 313.
179. Yarmolenko PS, Moon EJ, Landon C, Manzoor A, Hochman DW, Viglianti BL, Dewhirst MW. Thresholds for thermal damage to normal tissues: an update. Int. J. Hypertherm. 2011; 27(4): 320–343.
180. Oh S, Webb AG, Neuberger T, Park B, Collins CM. Experimental and numerical assessment of MRI-induced temperature change and SAR distributions in phantoms and in vivo. Magn. Reson. Med. 2010; 63(1): 218–223.
181. Oh S, Ryu YC, Carluccio G, Sica CT, Collins CM. Measurement of SAR-induced temperature increase in a phantom and in vivo with comparison to numerical simulation. Magn. Reson. Med. 2014; 71(5): 1923–1931.
182. Eryaman Y, Akin B, Atalar E. Reduction of implant RF heating through modification of transmit coil electric field. Magn. Reson. Med. 2011; 65(5): 1305–1313.
183. Etezadi-Amoli M, Stang P, Kerr A, Pauly J, Scott G. Controlling radiofrequency-induced currents in guidewires using parallel transmit. Magn. Reson. Med. 2014. DOI: 10.1002/mrm.25543
184. Langereis S, Keupp J, van Velthoven JL, de Roos IH, Burdinski D, Pikkemaat JA, Grull H. A temperature-sensitive liposomal 1H CEST and 19F contrast agent for MR image-guided drug delivery. J. Am. Chem. Soc. 2009; 131(4): 1380–1381.
185. Virtanen H, Huttunen J, Toropainen A, Lappalainen R. Interaction of mobile phones with superficial passive metallic implants. Phys. Med. Biol. 2005; 50(11): 2689.
186. Bakhai A, Booth J, Delahunty N, Nugara F, Clayton T, McNeill J, Davies S, Cumberland D, Stables R. The SV stent study: a prospective, multicentre, angiographic evaluation of the BiodivYsio phosphorylcholine coated small vessel stent in small coronary vessels. Int. J. Cardiol. 2005; 102(1): 95–102.
187. Ansems J, Kolk A, Kroeze H, Van den Berg NAT, Borst G, Luijten PR, Webb AG, Renema WKJ, Klomp DWJ. MR imaging of patients with stents is safe at 7.0 tesla. In Proceedings of the 20th Annual Meeting of ISMRM, Melbourne, Victoria, Australia; 2012: 2764.
188. Oberacker E, Winter L, Seifert F, Marek J, Weidemann G, Hoffmann E, Niendorf T. En route to ultrahigh field cardiac MR in patients: RF safety assessment of intracoronary stents at 7.0T using numerical simulations and E-field measurements. In *Proceedings of the Joint Meeting of ISMRM-ESMRB, Milan, Italy*. The International Society of Magnetic Resonance in Medicine, Berkeley, California, USA, 2014; 0177.
189. Eichfelder G, Gebhardt M. Local specific absorption rate control for parallel transmission by virtual observation points. Magn. Reson. Med. 2011; 66(5): 1468–1476.
190. Graessl A, Muhle M, Schwerter M, Rieger J, Oezerdem C, Santoro D, Lysiak D, Winter L, Hezel F, Waiczies S, Guthoff RF, Falke K, Hosten N, Hadlich S, Krueger PC, Langner S, Stachs O, Niendorf T. Ophthalmic magnetic resonance imaging at 7 T using a 6-channel transceiver radiofrequency coil array in healthy subjects and patients with intraocular masses. Invest. Radiol. 2014; 49(5): 260–270.
191. Lindner T, Langner S, Graessl A, Rieger J, Schwerter M, Muhle M, Lysiak D, Kraus O, Wuerfel J, Guthoff RF, Falke K, Hadlich S, Krueger PC, Hosten N, Niendorf T, Stachs O. High spatial resolution in vivo magnetic resonance imaging of the human eye, orbit, nervus opticus and optic nerve sheath at 7.0 Tesla. Exp. Eye Res. 2014; 125: 89–94.
192. Walter U, Niendorf T, Graessl A, Rieger J, Kruger PC, Langner S, Guthoff RF, Stachs O. Ultrahigh field magnetic resonance and colour Doppler real-time fusion imaging of the orbit – a hybrid tool for assessment of choroidal melanoma. Eur. Radiol. 2014; 24(5): 1112–1117.
193. Paul K, Graessl A, Rieger R, Lysiak D, Huelnhagen T, Winter L, Heidemann R, Lindner T, Hadlich S, Zimpfer A, Pohlmann A, Endemann B, Krüger PC, Langner S, Stachs O, Niendorf T. Diffusion-sensitized ophthalmic MRI free of geometric distortion at 3.0 T and 7.0 T: a feasibility study in healthy subjects and patients with intraocular masses. Invest. Radiol. 2015. DOI: 10.1097/RLI.0000000000000129
194. Poulo L, Alon L, Deniz C, Haefner R, Sodickson D, Stoeckel B, Zhu Y. A 32-channel parallel exciter/amplifier transmit system for 7T imaging. Proc. Int. Soc. Magn. Reson. Med. 2011; 19: 1867.
195. Gudino N, Heilman JA, Riffe MJ, Heid O, Vester M, Griswold MA. Oncoil multiple channel transmit system based on class-D amplification and pre-amplification with current amplitude feedback. Magn. Reson. Med. 2013; 70(1): 276–289.
196. Linz P, Santoro D, Renz W, Ruff J, Deimling M, Muller DN, Titze J, Luft FC, Niendorf T. Age dependent changes of sodium content in human calf skin measured with sub-millimeter spatial resolution 23Na MRI at 7.0 T. In *Proceedings of the 20th Annual Meeting of ISMRM, Melbourne, Victoria, Australia*. The International Society of Magnetic Resonance in Medicine, Berkeley, California, USA, 2012; 4372.
197. Umathum R, Rosler MB, Nagel AM. In vivo 39K MR imaging of human muscle and brain. Radiology 2013; 269(2): 569–576.
198. Nagel AM, Lehmann-Horn F, Weber MA, Jurkat-Rott K, Wolf MB, Radbruch A, Umathum R, Semmler W. In vivo ^{35}Cl MR imaging in humans: a feasibility study. Radiology 2014; 271(2): 131725.

199. Linz P, Santoro D, Renz W, Rieger J, Ruehle A, Ruff J, Deimling M, Rakova N, Mueller DM, Titze J, Luft FC, Niendorf T. Skin sodium measured with 23Na magnetic resonance imaging at 7.0 tesla. NMR Biomed. 2015; 28(1): 54–62.
200. Hoffmann SH, Radbruch A, Bock M, Semmler W, Nagel AM. Direct ^{17}O MRI with partial volume correction: first experiences in a glioblastoma patient. Magn. Reson. Mater. Phys. Biol. Med. 2014; 27 (6): 579–587.
201. Tian J, Shrivastava D, Strupp J, Zhang J, Vaughan JT. From 7T to 10.5T: B1+, SAR and temperature distribution for head and body MRI. In *Proceedings of the 20th Annual Meeting of ISMRM, Melbourne, Victoria, Australia*. The International Society of Magnetic Resonance in Medicine, Berkeley, California, USA, 2012; 2666.
202. Committee to Assess the Current Status and Future Direction of High Magnetic Field Science in the United States; Board on Physics and Astronomy; Division on Engineering and Physical Sciences; National Research Council. Washington, DC: National Academies Press, 2013.
203. Fu R, Brey WW, Shetty K, Gor'kov P, Saha S, Long JR, Grant SC, Chekmenev EY, Hu J, Gan Z, Sharma M, Zhang F, Logan TM, Bruschweller R, Edison A, Blue A, Dixon IR, Markiewicz WD, Cross TA. Ultra-wide bore 900 MHz high-resolution NMR at the National High Magnetic Field Laboratory. J. Magn. Reson. 2005; 177(1): 1–8.
204. Smeibidl P, Bird MD, Ehmler H, Tennant A. New hybrid magnet system for structure research at highest magnetic fields and temperatures in the millikelvin region. J. Phys. Conf. Ser. 2012; 400: 052034.
205. Manjon JV, Coupe P, Marti-Bonmati L, Collins DL, Robles M. Adaptive non-local means denoising of MR images with spatially varying noise levels. J. Magn. Reson. Imaging 2010; 31(1): 192–203.